International Journal of Earth Sciences (2023) 112:1553–1575
https://doi.org/10.1007/s00531-023-02313-6

ORIGINAL PAPER

Eocene to Late Oligocene extension dominated mafic magmatism from South Kaleybar, Iran

Mohammad Reza Ghorbani[1,2] · Mohammad Paydari[1] · Parham Ahmadi[1] · Albrecht von Quadt[3] · Vahid Ahadnejad[4] · John M. Cottle[5] · Ian T. Graham[2] · Jamshid Ahmadian[4] · Ahmad Ahmadvand[1]

Received: 1 April 2022 / Accepted: 15 April 2023 / Published online: 30 April 2023

Abstract

Vast and geochemically diverse volcanic rocks from the western Alborz Magmatic Assemblage (AMA) represent the back-arc of the central Iran Neotethyan arc (Urumieh–Dokhtar Magmatic Assemblage; UDMA). Volcanic rocks of the west AMA record valuable information on the timing, source region(s) and geodynamic setting of magmatism. Over 30 days of field study and sampling, investigation of 170 thin sections, 30 whole-rock geochemical analyses, 13 whole-rock Sr–Nd isotopic ratios and U–Pb age dating of zircon separates from 7 samples furnished the present study data. Eocene (38.5 Ma) OIB-type volcanic rocks from South Kaleybar indicate an anorogenic (extensional) setting. This lithospheric-scale extensional event induced influx of asthenospheric mantle into the sub-arc wedge, of which the partial melts differentiated to produce OIB-type melts. The OIB-type melts incorporated some inherited zircons in their ascent through the Cadomian crust. A continued extensional regime led to asthenospheric upwelling and produced mafic melts that produced 27.5-Ma-old subalkaline series volcanics. The LILE-depleted signature of the South Kaleybar subalkaline volcanic rocks implies that their mantle source region experienced previous partial melting event(s), probably during OIB-type magmatism in the Eocene. Alkaline volcanism (24.4 Ma) and concurrent high-silica adakitic volcanism (24.3 Ma–23.4 Ma) followed subalkaline magmatism. The alkaline rock signature in the study area range from 'Nb–Ta depleted' to 'plume-type'. This is consistent with lithosphere–asthenosphere interaction in an arc-related setting. Simultaneous partial melts of delaminated lower crustal rocks reacted with the asthenosphere and produced adakitic melts. Asthenospheric, lithospheric and crustal contribution to the magmatism in South Kaleybar express the back-arc signature of magmatism in Eocene to Late Oligocene times.

Keywords West Alborz magmatic assemblage · Neotethyan · Anorogenic · Eocene · Oligocene · OIB-type · Alkaline · Adakite · Subalkaline · Geochemistry · Back-arc

Introduction

As a segment of the Alpine–Himalayan Orogen, the western part of the Alborz Magmatic Assemblage (west AMA) that includes the study area, is one of the best representations of subduction-related, back-arc and collisional Cenozoic and Quaternary magmatism. The west Alborz Magmatic Assemblage provides an excellent opportunity for investigating the contribution of a variety of magmatic reservoirs including crustal, lithospheric mantle and asthenospheric mantle in the origin and evolution of the magmatism in a major convergence setting beneath the Iranian Plate in Mesozoic–Early Cenozoic times. The study area is surrounded by three tectonomagmatic units; (a) Lesser Caucasus, (b) Urumieh–Dokhtar Magmatic Assemblage (UDMA) and (c) Alborz Magmatic Assemblage towards

✉ Mohammad Reza Ghorbani
ghorbani@modares.ac.ir

[1] Department of Geology, Tarbiat Modares University, Tehran 14115-175, Iran

[2] Earth and Sustainability Sciences Research Centre, School of Biological, Earth and Environmental Sciences, The University of New South Wales, Sydney, NSW 2052, Australia

[3] Institute of Geochemistry and Petrology, ETH, 8092 Zurich, Switzerland

[4] Department of Geology, Payam-e-Noor University, Tehran, Iran

[5] Department of Earth Science, University of California, Santa Barbara, CA, USA

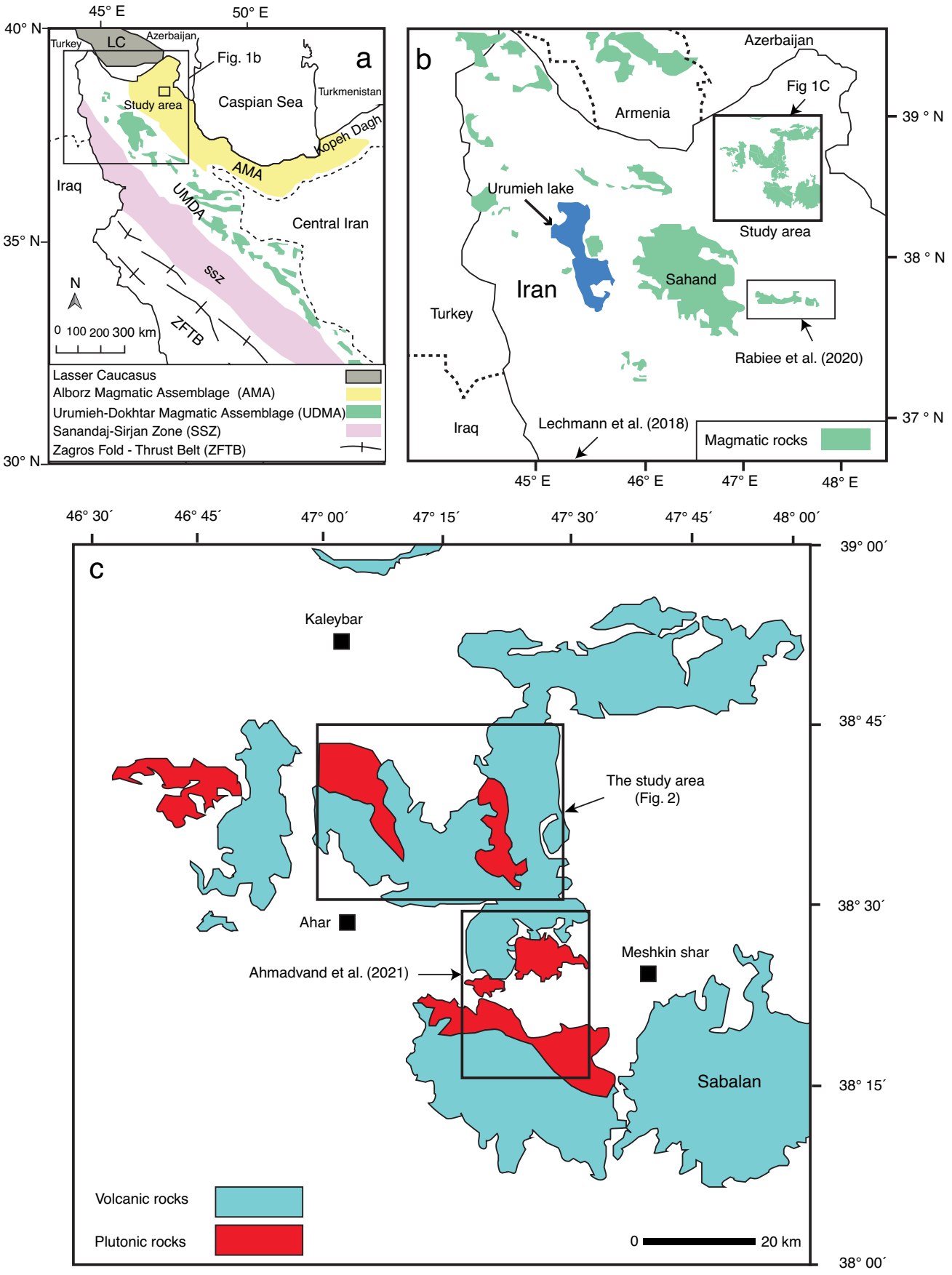
a
45° E
50° E
40° N
35° N
30° N
Turkey
LC
Azerbaijan
Fig. 1b
Study area
Caspian Sea
Turkmenistan
Kopeh Dagh
AMA
Iraq
UMDA
Central Iran
SSZ
ZFTB
N
0 100 200 300 km
Lasser Caucasus
Alborz Magmatic Assemblage (AMA)
Urumieh-Dokhtar Magmatic Assemblage (UDMA)
Sanandaj-Sirjan Zone (SSZ)
Zagros Fold - Thrust Belt (ZFTB)
b
Azerbaijan
Armenia
Fig 1C
Urumieh lake
Study area
Iran
Sahand
Turkey
Rabiee et al. (2020)
Iraq
Lechmann et al. (2018)
Magmatic rocks
39 ° N
38 ° N
37 ° N
45° E
46° E
47° E
48° E
c
46° 30´
46° 45´
47° 00´
47° 15´
47° 30´
47° 45´
48° 00´
39° 00´
38° 45´
38° 30´
38° 15´
38° 00´
Kaleybar
The study area
(Fig. 2)
Ahar
Meshkin shar
Ahmadvand et al. (2021)
Sabalan
Volcanic rocks
Plutonic rocks
0 20 km

◂**Fig. 1** **a** Major tectonomagmatic units and position of the study area shown on a map of Iran, **b** Magmatic rocks from NW Iran and **c** Distribution of volcanic and plutonic rocks in the study area and adjacent regions. The tectonomagmatic units are after Alavi (1996) and the Lesser Caucasus domain is from Rolland (2017)

NW, SW and SE, respectively (Fig. 1). The west Alborz Magmatic Assemblage is believed by most authors (e.g., Asiabanha and Foden 2012; Castro et al. 2013; Nabatian et al. 2014; Ahmadvand et al. 2021) to represent the back-arc system of the Central Iranian magmatic belt (i.e., the UDMA). The Urumieh–Dokhtar Magmatic Assemblage is the product of Cenozoic magmatism that followed the northward subduction of Neotethyan oceanic lithosphere beneath the Iranian Plate. A change in the angle of the subducting slab from the Paleocene to Oligocene prompted metasomatized lithospheric mantle wedge (i.e., that overlies Neotethyan oceanic slab) to melt. Gradual slab roll-back triggered asthenospheric mantle influx and an increased contribution to Oligocene–Miocene magmatism (Berberian and Berberian 1981; Moinvaziri 1985; Ghorbani 2006; Verdel et al. 2011; Ghorbani et al. 2014). While the main arc, the Urumieh–Dokhtar Magmatic Assemblage, is mainly of calc-alkaline character (Yeganehfar et al. 2013; Babazadeh et al. 2017), the back-arc, the west Alborz Magmatic Assemblage, contains a wide spectrum of subalkaline and alkaline rocks (Rabiee et al. 2020; Ahmadvand et al. 2021). Adakitic rocks are reported from both the Urumieh–Dokhtar Magmatic Assemblage (Ghorbani and Bezenjani 2011; Omrani et al. 2008) and the west Alborz Magmatic Assemblage (Jahangiri 2007; Ahmadvand et al. 2021). Ahmadvand et al. (2021) introduced both A-type and high-Nb volcanic rocks from the west Alborz Magmatic Assemblage; these rocks were regarded as implying an asthenospheric mantle contribution in a back-arc, extensional framework.

The aims of present study are to: (a) understand the field relationship of the rock sequences from the west Alborz Magmatic Assemblage; (b) study the textural, mineralogical and geochemical variations of the volcanic rocks from the west Alborz Magmatic Assemblage; and (c) present a geodynamic model that explains the formation and evolution of the magmas from their source regions to the site of their emplacements.

Geology of the study area

As noted earlier, the west Alborz Magmatic Assemblage is interpreted to represent a back-arc situation and a northeast extensional region of the major Neotethyan magmatic arc (i.e., UDMA; Fig. 1a). Lithospheric thickness decreases from the Urumieh–Dokhtar Magmatic Assemblage towards the northeast (Shad Manaman et al. 2011); this attests to the extension and supports a back-arc position for the west Albroz Magmatic Assemblage. Two studies have been carried out on the volcanic rocks from the southern (Rabiee et al. 2020) and western (Lechmann et al. 2018) parts of the study area (Fig. 1b). Rabiee et al. (2020) investigated the Mianeh–Hashtrud polyphase magmatism from 45 to 6 Ma. The polyphase magmatism was found to be dominated by intermediate to felsic volcanic rocks of calc-alkaline to shoshonitic affinity which have been derived from the partial melting of underplated mafic rocks. Activation of the lithospheric boundary was suggested to have triggered this magmatism. The study of Lechmann et al. (2018) covered a large area across the western part of the west Alborz Magmatic Assemblage and reported two age clusters, at 16.2 Ma and 5.5 Ma. Shoshonitic alkali basalts to felsic rocks and low-K to calc-alkaline intermediate to felsic rocks from this large area have arc-signatures (Nb–Ta negative anomaly) that were considered as representing heterogeneous metasomatized mantle (Lechmann et al. 2018). The Eocene to Miocene volcanic successions south-east of Ahar (i.e., towards the south of the study area; Fig. 1) include the first A-type and high-Nb magmatism reported from the west AMA (Ahmadvand et al. 2021).

The Khankandi, Shivardagh, Youseflu and Mizan plutonic bodies build a significant portion of the Cenozoic magmatism in the west Alborz Magmatic Assemblage (Fig. 1c). Previous zircon U–Pb age dating (Aghazadeh et al. 2010, 2011; Castro et al. 2013) and whole-rock geochemical data of these plutonic bodies revealed dates between 23 and 31 Ma and the existence of granite, granodiorite to monzonite, monzogabbro and gabbro. All these rocks were attributed to the partial melting of mantle metasomatized by slab fluids (Aghazadeh et al. 2010, 2011). An adakitic signature for some of these intrusive bodies have been regarded as indicating slab melts involvement in metasomatism of the source mantle (Castro et al. 2013). Nabatian et al. (2014) believed that melts from the underlying mantle heated the overlying crustal rocks to produce I-type granitic bodies near Zanjan.

The investigated area mainly comprises Eocene to Late Oligocene successions (Figs. 2, Online Resource 1). The oldest strata that crop out near the study area include Cretaceous sedimentary beds and interlayered volcanic strata. However, the presence of older basement rocks is implied by the inherited zircons found in the magmatic rocks from the present study. The crystalline basement is regarded as part of the Cadomian magmatic arc which resulted from the subduction of Prototethys beneath the northern margin of Gondwana (Chiu et al. 2018).

The Eocene to Late Oligocene volcanic successions from the study area are altered to varying degrees and appear as isolated outcrops. The outcrops constitute pale gray to brownish and black volcanic rocks/beds of up to a

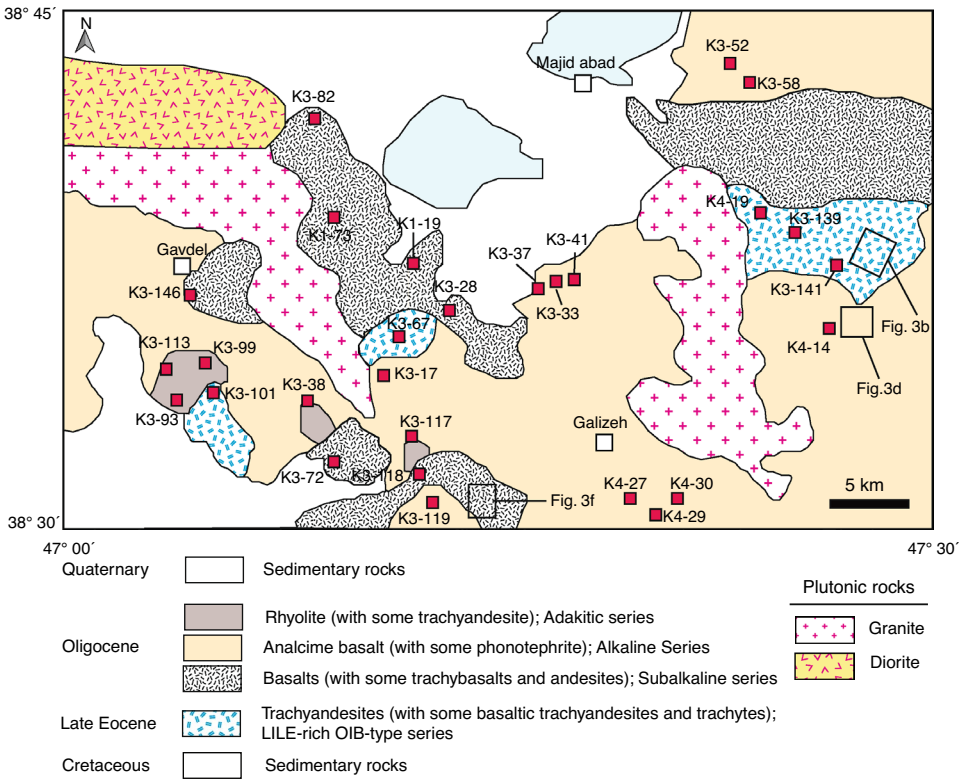

Fig. 2 Geological map of the study area in South Kaleybar (Paydari 2023) with major modifications after Emami (2000)

few meters thickness. Hence, the field relationships of the volcanic units are not conclusive. The original volcanic successions are only maintained in limited scales in some parts of the study area (Online resource 1). The Eocene–Oligocene units include basaltic, andesitic, trachyandesitic and phonotephritic rocks that mainly occur as lavas and trachytic rocks that mainly occur as dykes and domes. Widespread hydrothermal alterations are due to the emplacement of multiple plutonic bodies and volcanic pulses (Fig. 1) of Eocene to Miocene age in the study area and adjacent regions (e.g., Nabatian et al. 2014; Ahmadvand et al. 2021).

Sampling and analytical methods

Sampling

The sampling strategy of the volcanic rock units was based on the Kaleybar 1:100:000 geological map (Emami 2000). Endeavors were made to sample all the volcanic lithologies present. A collection of 220 samples was gathered from the study area, 170 of which were selected for thin-sectioning. Measures adopted for sample sectioning were: their degree of freshness, mineralogical and textural varieties, geographical distribution and presumed relative ages in the volcanic succession. See Online Resource 2 for the details of samples from South Kaleybar selected to obtain the geochemical data. 30 of the volcanic rocks which show the least alteration effects and represent different textural and mineralogical suites from the study area were selected for whole-rock major- and trace-element analysis.

Zircon U–Pb geochronology and trace elements

Zircon U–Pb age dating on 7 samples (Online Resource 3) were carried out on two different occasions. Four samples (K3-130, K3-113, K3-93 and K4-38) were analyzed at ETH Zurich, while three samples (K1-19, K3-82 and K4-19) were analyzed at the University of Santa Barbara, California. Zircon separates were prepared using standard crushing, heavy liquid, and isodynamic separation techniques at the Tarbiat Modares University, Tehran.

Methods at ETH Zurich: Spatially resolved in situ U–Pb age and trace-element analyses on zircons were carried out simultaneously on the same zircon volumes using a 193 nm S155-LR ASI Resolution Excimer laser ablation system coupled with a Thermo Scientific Element-XR sector-field (SF)-ICP-MS. Weighted mean ^{206}Pb-^{238}U dated and substantial uncertainties were calculated using the open-source online toolbox IsoplotR v4.15 (Ludwig 2012). The weighted mean ^{206}Pb–^{238}U dates are reported with two uncertainties; the first is calculated as the 2σ statistical uncertainty from the weighted mean, and the second with a propagated systematics external uncertainty of 1.5% (Horstwood et al. 2016). The data reduction followed the approach proposed

by Vermeesch (2021). Further details can be found in the Online Resource 4.

Methods at the University of Santa Barbara, California: Zircon U–Pb geochronology was acquired using a laser ablation 'split stream' setup consisting of a Photon Machines Excimer 193 nm laser ablation unit coupled to a Nu Instruments, 'Nu Plasma' multi-collector ICP-MS (Cottle et al. 2011; 2013; Kylander-Clark et al. 2013; with modifications as described in McKinney et al. 2015). The uncertainty on the ^{207}Pb corrected age incorporates uncertainties on the measured ^{206}Pb/^{238}U and ^{207}Pb/^{206}Pb ratios as well as 1% uncertainty on the assumed common lead composition. "91500" zircon (Wiedenbeck et al. 1995) served as the primary reference material, while GJ-1 zircon (Jackson et al. 2004) was treated as an unknown in order to assess accuracy and precision. Weighted mean plots were calculated in IsoPlot v4.15 (Ludwig 2012) using the ^{238}U and ^{235}U decay constants of Steiger and Jager (1977). Data reduction was carried out using Iolite v3.5 (Paton et al. 2010). Further details can be found in the Online Resource 5.

Major-and trace-element analyses

Whole-rock major- and trace-element analyses were carried out on fused glass beads prepared from starting 35–50 g pieces of rock samples. Rock pieces were first crushed and then pulverized in a tungsten carbide vessel using an oscillatory mill. The rock powder was then placed in a warm cabinet overnight at 108 °C to eliminate adsorbed weakly bound water. Powder aliquot of 1.5 g of each sample was transferred into ceramic crucibles and heated in an oven at 1050 °C for 2 h to determine the loss on ignition (LOI). LOI was calculated as the mass difference of the sample before and after heating. After cooling, aliquots were blended and homogenized with a fluxer agent mixture of 66% Li-tetraborate ($Li_2B_4O_7$) and 34% Li-metaborate ($LiBO_2$) in 1:5 proportion. Alternatively, 100% Li-tetraborate was used in 1:6 proportion for glass bead that fractured repeatedly after cooling. The homogenized mixtures were placed in Pt–Au crucibles and loaded into a Panalytical Claisse Eagon 2 fully automated fusion instrument at 1050 °C for ~ 20 min to produce fused glass beads.

Major element oxide concentrations were measured using a Panalytical Axios X-ray fluorescence (XRF) instrument equipped with a sequential wavelength-dispersive spectroscopy (WDS) detector at ETH Zurich, Switzerland. The XRF instrument was calibrated using 35 internationally accepted standard powders processed to glass beads. Operating acceleration voltage of 24–60 kV and electric current of 40–100 mA was applied.

Trace-element concentrations were analyzed on glass-bead shards using a 193 nm GeoLas (Coherent, Germany) Excimer laser system coupled to a NexION 2000 (Perkin-Elmer, USA/Canada) fast-scanning quadrupole inductively coupled-plasma mass spectrometer (ICP-MS) at ETH Zurich, Switzerland. Each analysis consisted of ~ 30 s of gas blank acquisition followed by ~ 40 s of sample ablation. The carrier gas consisted of high-purity helium (ca. 1 L min^{-1}) to which argon (ca. 1 L min^{-1}) was admixed downstream of the ablation cell. NIST SRM 610 served as the primary reference material for calibration and instrumental sensitivity drift correction, while USGS BCR-2 was used as the secondary reference material for accuracy and reproducibility control.

Blank glass made of Li-meta-/tetraborate mixture was analyzed for blank (interference) correction. Standard operating conditions of the laser system were an energy density (i.e., fluence) of 10 J cm^{-2} and a repetition rate of 10 Hz. Glass-beads from rock samples and BCR-2, and blank glass were ablated with a 115 µm spot-size applying an acceleration voltage of 26 kV. NIST SRM 610 glass beads were ablated with a 40 µm spot-size applying 24 kV. Reference materials and glass blank were analyzed in a conventional standard-sample bracketing procedure at the start and end of each session, and between each block of five sample glass beads. Each glass bead was measured three consecutive times. Data reduction, including corrections for time-dependent instrumental drift, matrix interferences, and relative sensitivity, and calculation of element concentrations was done using the MATLAB-based software SILLS (Guillong et al. 2008). CaO concentrations measured by XRF were used as an internal standard except in cases where CaO < 1 wt% for which SiO_2 was used. Matrix interferences were corrected with the stoichiometric Li concentration in Li-tetraborate (80 500 µg g^{-1}) used in the fluxer agent. Data from three analyses of each sample glass bead were averaged to obtain the final whole-rock trace-element concentrations (Table 1).

Sr–Nd isotope analyses

The Sr and Nd isotopic data of 13 samples (Table 2) were obtained at ETH Zurich, Switzerland. Details of the analytical techniques, taking into account their accuracy and precision can be found in von Quadt et al. (1999). Whole-rock powders of 10–40 mg were digested in HF and HNO_3; Nd and Sr were separated by ion-exchange chromatography techniques in 100 µl TEP columns (Pin et al. 1994) with Sr-Spec, TRU-Spec and LnSpec (Eichrom resin®). Sr was loaded with a Ta emitter on Re filaments; Nd was loaded with 2 n HCL on Re filaments. Both isotopes were analyzed on a Thermo Scientific TritonPlus mass spectrometer operated in static mode measurements. The measured ^{87}Sr/^{86}Sr ratios were normalized to an ^{87}Sr/^{86}Sr value of 8.37521. The mean ^{87}Sr/^{86}Sr value of the NBS 987 standard obtained during the period of measurements was 0.710252 ± 12 (2 σ,

Table 1 Major elements (wt %) and trace elements (ppm) contents of the volcanic rocks from South Kaleybar

Rock type	OIB-type					Subalkaline series							Alkaline series		
Sample	K3-67	K3-101	K3-139	K3-141	K4-19	K1-19	K3-28	K3-72	K3-73	K3-82	K3-106	K3-118	K3-33	K3-41	K3-37
Major element (wt. %)															
SiO_2	64.8	61.0	55.5	61.7	54.4	58.9	55.2	52.1	63.3	48.3	48.2	48.3	54.4	49.2	49.4
TiO_2	0.5	0.9	0.7	0.5	0.9	0.8	0.9	2.1	1.4	2.2	2.0	1.4	0.9	0.7	0.8
Al_2O_3	20.3	19.8	21.2	21.2	20.1	17.9	19.1	16.8	16.1	16.4	15.3	17.8	18.7	18.0	18.3
Fe_2O_3	2.3	4.6	5.1	2.9	6.1	5.4	8.9	11.8	7.5	10.2	11.2	10.5	8.5	9.4	10.1
MnO	0.0	0.0	0.1	0.1	0.2	0.1	0.2	0.2	0.1	0.1	0.2	0.1	0.2	0.2	0.3
MgO	0.3	0.6	2.2	0.5	2.4	2.6	3.3	4.1	3.0	5.5	7.5	5.7	2.4	4.3	4.1
CaO	0.5	3.9	5.3	2.7	5.8	7.0	7.6	5.2	2.4	11.3	11.7	12.1	4.7	9.3	8.7
Na_2O	5.8	4.3	3.9	4.5	4.2	5.0	4.0	6.2	5.3	3.5	2.6	3.3	4.9	3.1	4.6
K_2O	5.6	4.4	5.5	5.7	5.5	1.7	0.5	0.7	0.6	1.1	0.8	0.2	4.6	5.2	3.3
P_2O_5	0.1	0.5	0.4	0.1	0.5	0.4	0.5	0.8	0.4	1.5	0.7	0.6	0.7	0.6	0.4
LOI	1.7	1.6	3.1	3.8	2.9	0.9	5.0	3.8	3.0	2.1	4.4	5.2	4.5	3.4	8.0
Trace element (ppm)															
Ga	20.1	20.6	21.5	21.6	22.0	20.0	14.9	15.8	15.9	21.8	16.6	17.8	16.1	13.6	14.9
Cs	3.0	2.2	5.5	5.8	2.4	0.4	0.8	1.2	1.5	1.6	2.8	3.7	0.8	37.5	1.1
Rb	166	137	153	100	115	20	9	16	13	7	5	3	87	97	76
Ba	243	834	1180	638	1290	555	342	238	220	1171	547	553	1202	1992	841
Th	39.4	28.2	30.2	42.0	38.7	6.1	5.6	3.9	4.1	13.1	2.9	5.1	6.6	9.8	3.0
U	13.1	8.8	9.4	10.8	10.9	1.6	1.5	0.5	1.2	2.4	0.7	1.3	2.2	3.4	0.7
Nb	52.9	32.0	44.0	62.3	49.7	14.4	13.4	37.4	17.9	52.8	16.1	18.8	4.3	7.0	3.2
Ta	3.2	2.0	2.3	3.4	2.5	0.7	0.7	2.2	1.2	2.4	0.9	1.0	0.3	0.4	0.2
La	82.9	73.5	85.1	88.2	117.2	39.1	40.4	40.8	30.4	87.3	30.0	42.5	31.2	36.9	18.3
Ce	146	127	151	160	190	68	70	81	55	167	60	82	60	67	34
Pb	16.7	17.2	29.1	36.4	22.5	9.7	7.0	4.1	9.2	9.3	4.0	9.0	7.3	27.2	2.5
Pr	13.7	13.7	15.1	15.4	20.2	7.1	8.1	9.3	6.6	19.2	7.4	9.6	7.2	7.6	4.2
Sr	316	792	1829	676	1686	1164	877	460	445	2269	794	1134	1018	1181	592
Nd	45.8	51.7	50.7	49.3	75.9	24.4	33.3	37.7	27.8	74.2	32.2	39.4	32.0	31.2	18.9
Hf	10.8	7.5	5.1	7.5	8.3	2.4	3.6	4.6	3.8	4.7	3.4	3.3	3.1	1.6	1.6
Sm	7.3	9.4	8.1	7.7	12.8	3.8	6.0	7.4	5.8	11.3	6.4	7.6	6.6	6.3	4.1
Tl	0.7	0.3	0.3	0.3	0.2	0.0	0.0	b.d	0.1	0.3	0.0	b.d	0.3	0.3	0.0
Gd	4.6	8.4	5.4	5.0	9.4	2.6	5.2	6.5	5.2	7.5	5.8	6.3	5.7	5.3	4.1
Tb	0.7	1.3	0.7	0.7	1.1	0.3	0.7	0.9	0.9	0.8	0.8	0.9	0.8	0.7	0.6
Dy	3.5	7.0	3.4	3.5	5.6	1.5	3.8	4.9	5.0	4.0	4.2	4.4	3.9	3.5	3.3
Ho	0.7	1.4	0.6	0.7	1.0	0.3	0.7	1.0	1.1	0.7	0.8	0.9	0.7	0.6	0.7
Er	2.1	3.5	1.6	1.8	2.7	0.7	1.9	2.5	2.9	1.5	2.1	2.2	2.3	1.6	1.7
Tm	0.3	0.5	0.2	0.2	0.4	0.1	0.3	0.4	0.5	0.2	0.3	0.3	0.3	0.2	0.3

Table 1 (continued)

Rock type	OIB-type					Subalkaline series							Alkaline series		
Sample	K3-67	K3-101	K3-139	K3-141	K4-19	K1-19	K3-28	K3-72	K3-73	K3-82	K3-106	K3-118	K3-33	K3-41	K3-37
Yb	2.6	3.5	1.5	2.0	2.4	0.6	2.0	2.2	2.9	1.1	1.7	2.0	2.1	1.4	1.8
Lu	0.4	0.6	0.2	0.3	0.4	0.1	0.3	0.3	0.5	0.2	0.3	0.3	0.3	0.2	0.3
Y	21.1	41.5	16.8	18.3	28.0	7.6	20.8	24.8	29.6	17.2	20.8	22.2	20.9	17.0	18.1
Sc	3.3	14.4	5.6	2.7	7.5	10.0	16.2	21.5	18.4	17.7	29.0	25.5	10.6	14.5	19.2
V	70	165	126	87	177	152	155	138	159	247	261	276	252	285	224
Cr	23	50	33	26	31	63	33	202	34	114	325	45	34	60	54
Co	2.5	13.7	11.3	2.0	12.7	15.2	24.7	17.1	16.6	29.8	35.8	28.3	18.6	39.5	22.5
Ni	7.2	13.2	14.8	7.6	9.5	26.4	14.3	74.0	11.0	60.7	96.7	33.0	11.7	20.9	13.1
CIPW Norm															
Nepheline			1.3		5.3								3.6	11.5	11.8
Olivine			7.5		6.7			13.1		9.4	7.6	10.1	9.2	8.2	8.2
Quartz	7.7	9.1		5.6		5.6	6.3		18.2						
Anorthite	1.5	16.2	22.8	12.1	19.2	21.1	30.9	15.3	8.9	25.2	26.4	31.0	14.5	18.8	17.5
Albite	47.6	35.5	29.0	36.6	24.1	41.6	31.6	49.0	43.2	28.3	20.6	26.3	32.9	3.9	14.0
Orthoclase	32.0	25.5	31.1	32.0	31.5	9.8	2.7	4.1	3.1	6.1	4.6	1.2	25.6	29.5	17.9
Diopside					4.6	8.3	1.3	3.6		16.1	19.8	17.9	2.7	17.5	16.1
Hypersthene	2.6	5.3		4.0		7.3	15.7		13.3	0.7	7.0				

Rock type	Alkaline series									Adakitic rocks					
Sample	K3-119	K4-14	K4-27	K4-29	K3-17	K3-52	K3-58	K3-130	K4-30	K3-78	K3-93	K3-99	K3-113	K3-117	K4-38
Major element (wt %)															
SiO_2	54.8	51.4	50.4	49.1	51.9	55.3	55.8	58.8	55.9	75.2	58.9	64.1	63.0	62.1	65.7
TiO_2	0.9	1.1	1.5	2.0	1.0	0.5	0.5	0.9	0.9	0.9	0.9	0.8	1.0	0.8	0.6
Al_2O_3	18.8	17.7	18.6	16.2	19.3	22.8	21.5	17.2	18.6	17.0	16.2	18.6	18.3	17.6	16.6
Fe_2O_3	7.5	9.8	9.1	9.9	8.6	3.9	3.4	6.0	7.3	3.3	5.8	3.9	5.1	5.6	4.3
MnO	0.1	0.2	0.1	0.2	0.3	0.2	0.2	0.2	0.1	0.1	0.1	0.0	0.0	0.1	0.0
MgO	3.2	3.9	4.9	7.3	3.5	2.0	1.1	2.8	2.7	0.4	3.5	0.6	0.4	1.3	1.0
CaO	7.3	8.1	8.5	9.6	7.1	4.5	5.3	5.0	6.0	1.6	6.4	3.3	3.0	6.6	3.2
Na_2O	4.4	4.9	3.9	2.9	3.8	5.8	6.2	4.9	5.1	0.0	4.0	4.3	4.3	3.8	4.2
K_2O	2.2	2.0	2.1	2.0	3.7	4.7	5.9	3.7	2.7	1.0	3.8	4.1	4.3	2.0	4.1
P_2O_5	0.6	0.9	0.8	0.8	0.8	0.3	0.2	0.5	0.6	0.5	0.4	0.3	0.6	0.2	0.2
LOI	3.6	3.5	2.2	2.9	4.6	6.3	8.1	1.5	5.3	6.8	1.1	1.4	1.5	4.2	1.0
Trace element (ppm)															
Ga	19.0	16.7	20.1	17.7	18.8	16.2	12.6	16.6	18.6	17.9	19.8	19.4	15.3	19.0	16.3
Cs	1.0	0.7	1.9	0.9	1.9	2.8	3.1	3.9	2.6	1.5	4.0	2.1	2.2	3.0	2.0

Table 1 (continued)

Rock type	Alkaline series									Adakitic rocks					
Sample	K3-119	K4-14	K4-27	K4-29	K3-17	K3-52	K3-58	K3-130	K4-30	K3-78	K3-93	K3-99	K3-113	K3-117	K4-38
Rb	45	43	31	30	74	73	167	60	55	96	120	104	59	89	111
Ba	932	740	912	820	2333	1459	2382	646	1609	869	906	970	663	1063	914
Th	6.8	4.1	5.4	4.0	10.6	11.5	10.4	8.6	14.9	17.4	11.7	16.2	14.8	14.6	17.2
U	2.1	1.1	1.5	0.9	3.2	1.5	2.3	2.3	4.2	5.1	3.3	3.5	5.1	2.7	3.6
Nb	16.4	12.9	20.8	34.2	14.2	16.1	11.9	14.9	20.4	18.2	17.8	25.3	29.2	21.9	21.3
Ta	0.9	0.7	1.1	2.1	0.8	0.9	0.7	1.0	1.4	1.2	1.2	1.8	1.8	1.5	1.7
La	52.6	39.0	56.3	46.5	60.0	39.0	42.8	50.6	43.1	54.9	36.3	48.9	44.3	55.1	46.9
Ce	97.6	73.4	104.3	86.6	104.3	66.8	72.1	88.1	84.0	95.2	64.9	83.1	78.8	98.7	72.5
Pb	7.8	9.9	8.6	5.5	13.9	19.7	26.4	8.4	19.3	15.4	11.9	14.8	15.9	24.6	15.8
Pr	10.5	8.8	11.6	10.1	11.8	7.0	7.7	9.7	8.7	10.3	7.0	9.0	7.9	10.9	7.3
Sr	1285	1724	1316	1172	1212	1208	883	905	118	1025	841	926	822	1009	680
Nd	40.4	37.6	47.8	41.5	47.1	26.9	29.5	38.6	31.6	40.6	26.9	34.7	27.2	39.3	26.4
Hf	3.5	2.9	3.9	4.1	4.3	2.8	2.7	3.9	3.5	4.5	3.9	5.0	3.8	5.2	4.6
Sm	6.7	7.4	8.1	7.5	8.6	5.0	5.5	6.8	4.8	7.0	4.6	5.9	4.5	6.8	4.1
Tl	0.1	0.0	0.1	0.0	0.2	0.2	0.3	0.1	0.8	0.2	1.0	0.4	0.2	0.2	0.2
Gd	5.1	6.1	6.7	6.1	6.5	3.8	4.2	5.3	3.4	5.2	3.3	4.1	3.2	4.7	3.3
Tb	0.7	0.8	0.8	0.8	0.8	0.5	0.6	0.6	0.4	0.6	0.4	0.5	0.4	0.6	0.4
Dy	3.4	4.4	4.0	4.2	4.2	2.8	3.0	3.6	2.1	3.0	2.2	2.5	2.3	2.8	2.2
Ho	0.6	0.8	0.7	0.8	0.8	0.6	0.6	0.7	0.4	0.6	0.4	0.4	0.5	0.5	0.4
Er	1.7	2.0	1.7	1.9	2.1	1.4	1.5	1.8	0.9	1.4	1.0	1.1	1.2	1.5	1.2
Tm	0.2	0.3	0.3	0.3	0.3	0.2	0.2	0.2	0.1	0.2	0.1	0.1	0.2	0.2	0.2
Yb	1.6	2.0	1.6	1.7	1.8	1.5	1.7	1.7	1.0	1.3	0.9	0.8	1.3	1.4	1.1
Lu	0.2	0.3	0.2	0.3	0.3	0.2	0.2	0.3	0.1	0.2	0.1	0.1	0.2	0.2	0.2
Y	17.1	21.6	20.0	21.2	21.5	14.6	16.8	17.7	10.0	15.6	10.1	10.4	11.6	15.0	11.8
Sc	13.3	13.4	17.4	19.8	12.0	3.8	2.5	7.6	8.6	12.9	9.4	9.4	7.9	10.0	8.7
V	193	294	236	207	228	173	133	151	125	157	125	141	146	155	116
Cr	53	28	55	325	20	27	22	20	127	108	76	70	41	53	62
Co	19.3	22.0	25.4	31.5	20.1	6.7	4.5	13.9	3.9	15.7	11.5	7.6	10.0	15.7	8.1
Ni	23.8	11.9	32.8	153.0	10.8	8.0	10.3	9.2	27.3	43.1	39.0	83.2	11.6	40.5	18.5
CIPW Norm															
Nepheline		3.5	0.7		1.6	8.2	14.9								
Olivine		9.8	11.9	11.3	10.7	6.2	1.0		2.7						
Quartz								1.4		62.4	4.1	14.5	14.0	15.0	15.7
Anorthite	23.5	19.6	26.3	24.6	23.0	18.9	12.8	13.4	18.9	4.3	15.0	14.0	11.1	23.5	14.1
Albite	35.6	32.9	30.6	23.2	27.6	30.2	20.7	40.4	40.2	0.1	33.0	35.5	35.5	30.0	35.1

Table 1 (continued)

Rock type	Alkaline series									Adakitic rocks					
Sample	K3-119	K4-14	K4-27	K4-29	K3-17	K3-52	K3-58	K3-130	K4-30	K3-78	K3-93	K3-99	K3-113	K3-117	K4-38
Orthoclase	12.6	11.0	12.1	11.2	20.8	25.5	32.1	21.6	14.8	5.3	21.8	23.9	24.9	11.2	23.6
Diopside	6.2	11.0	7.5	13.0	4.0		8.6	6.4	4.3		10.8			4.6	0.1
Hypersthene	11.5			3.8				9.4	7.3	3.3	8.5	4.6	5.2	5.8	6.4

Table 2 Sr–Nd isotopic analyses of the volcanic rocks from S Kaleybar

Rock type	U/Pb mean age (Ma)	Sample	Rb (ppm)	Sr (ppm)	$^{87}Rb/^{86}Sr$	$^{87}Sr/^{86}Sr$ (measured)	±2 s.e	$(^{87}Sr/^{86}Sr)i$	±2 s.e	Sm (ppm)	Nd (ppm)	$^{147}Sm/^{144}Nd$	$^{143}Nd/^{144}Nd$ (measured)	±2se	$(^{143}Nd/^{144}Nd)i$	±2 s.e
OIB-type	38.5 ± 2.5	K3-101	136.5	792.4	0.4862	0.704752	0.000009	0.704490	0.000033	9.38	51.73	0.1142	0.512701	0.000013	0.512672	0.000017
Subalkaline	27.49 ± 0.40	K1-19	19.7	1163.7	0.0477	0.704205	0.000011	0.704187	0.000011	3.76	24.43	0.0968	0.512564	0.000007	0.512547	0.000007
		K3-28	9.3	876.6	0.0298	0.704357	0.000026	0.704346	0.000026	6.00	33.33	0.1134	0.512569	0.000006	0.512549	0.000007
		K3-73	13.4	444.5	0.0852	0.706069	0.000015	0.706036	0.000016	5.84	27.80	0.1322	0.512441	0.000005	0.512417	0.000006
		K3-106	5.2	794.1	0.0183	0.704475	0.000019	0.704468	0.000019	6.37	32.17	0.1248	0.512579	0.000011	0.512557	0.000012
Alkaline	24.37 ± 0.13	K3-33	87.0	1017.7	0.2412	0.705325	0.000055	0.705243	0.000056	6.62	32.00	0.1304	0.512672	0.000013	0.512651	0.000013
		K3-41	97.3	1180.7	0.2327	0.705519	0.000013	0.705440	0.000014	6.30	31.23	0.1270	0.512529	0.000008	0.512509	0.000008
		K3-37	76.4	591.5	0.3647	0.706172	0.000028	0.706048	0.000029	4.08	18.90	0.1359	0.512625	0.000006	0.512603	0.000006
		K4-27	31.2	1315.7	0.0670	0.704672	0.000018	0.704649	0.000018	8.11	47.77	0.1070	0.512728	0.000009	0.512711	0.000009
		K3-58	167.0	883.4	0.5337	0.705181	0.000008	0.704999	0.000009	5.49	29.47	0.1174	0.512542	0.000011	0.512523	0.000011
Adakite	23.68 ± 0.13	K3-93	95.9	1025.0	0.2642	0.704593	0.000018	0.704506	0.000019	7.04	40.57	0.1093	0.512713	0.000004	0.512696	0.000004
	23.38 ± 0.13	K3-113	103.6	926.0	0.3159	0.705054	0.000023	0.704951	0.000025	5.88	34.67	0.1069	0.512761	0.000014	0.512744	0.000014
	24.32 ± 0.12	K4-38	111.4	680.3	0.4624	0.705001	0.000018	0.704844	0.000018	4.09	26.40	0.0975	0.512761	0.000009	0.512745	0.000009

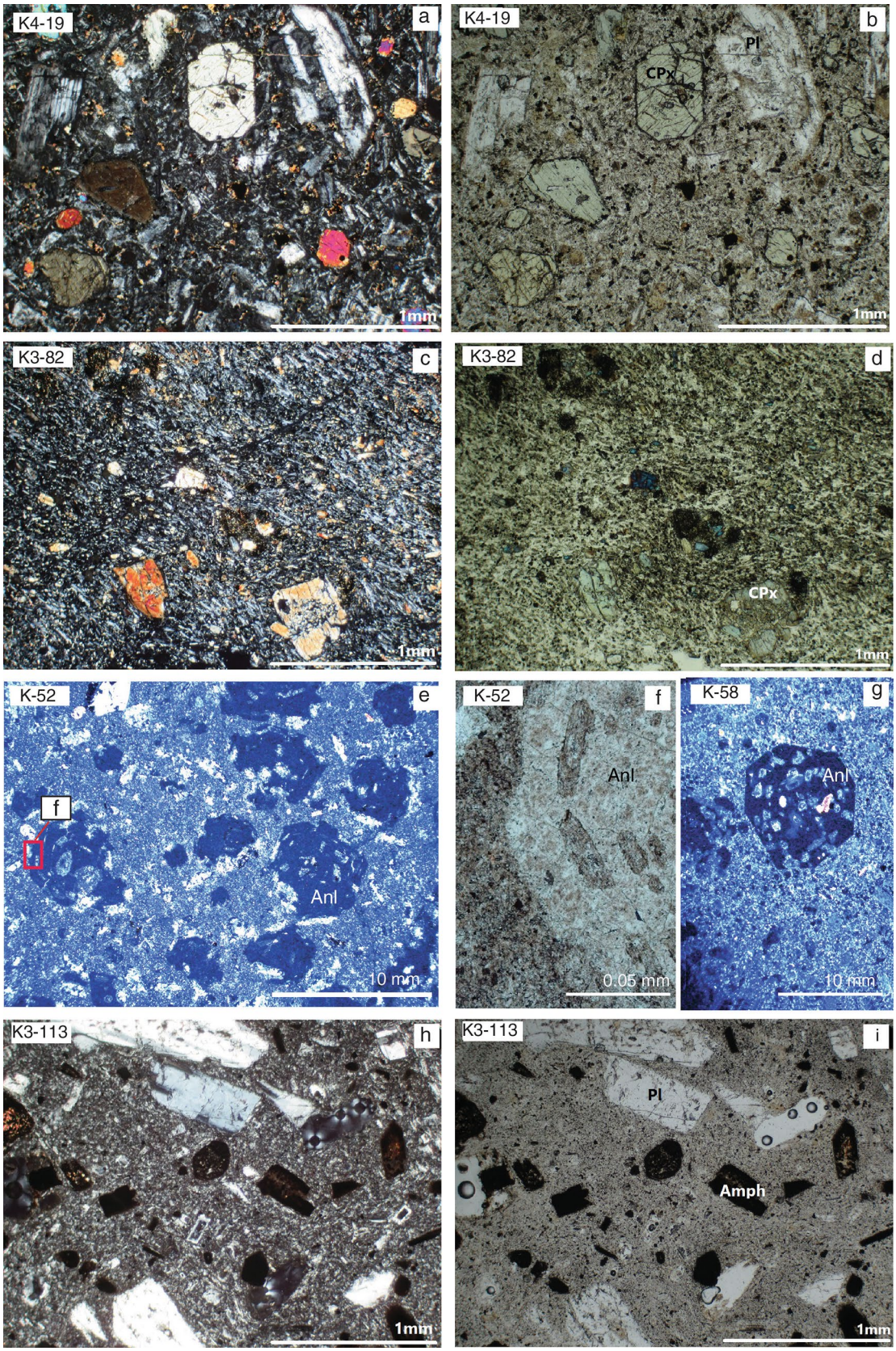
K4-19
a
1mm
K4-19
b
Pl
CPx
1mm
K3-82
c
1mm
K3-82
d
CPx
1mm
K-52
e
f
Anl
10 mm
K-52
f
Anl
0.05 mm
K-58
g
Anl
10 mm
K3-113
h
1mm
K3-113
i
Pl
Amph
1mm

◂**Fig. 3** **a**, **b** Plagioclase and clinopyroxene phenocrysts and microphenocrysts set in a groundmass mainly composed of glass and minor amounts of plagioclase and opaque (Fe–Ti oxides) in a trachyandesite, **c**, **d**) Clinopyroxene and olivine pseudomorphs set in a cryptocrysltalline groundmass composed of feldspar laths, some clinopyroxene, opaque (Fe–Ti oxides) and glass in a subalkali basalt–andesite, **e** Analcime phenocrysts and feldspar microphenocrysts set in a vitrophyric groundmass mainly composed of glass and some minute feldspars in an analcime basalt–andesite, **f** Magnified view of an analcime crystal that poikilitically encloses feldspar crystals (see Fig. 3e; general view of this sample) in an analcime basalt–andesite, **g** A euhderal analcime phenocryst that poikilitically encloses feldspar and clinopyroxene crystals in an analcime basalt–andesite. The rock groundmass consists of glass with minute feldspars and clinopyroxene crystals, **h**, **i** Plagioclase and opacitized amphibole phenocrysts set in a cryptocrystalline groundmass comprising glass, feldspar and opaques (Fe–Ti oxides) in an amphibole-biotite trachyte. photomicrographs **a**, **c**, **e**, **g**, **h** are in crossed polarized light (xpl) and **b**, **d**, **f**, **i** are in plane polarized light (ppl)

n = 18). The measured $^{143}Nd/^{144}Nd$ ratios were normalized to the $^{146}Nd/^{144}Nd$ value of 0.7219. The mean $^{143}Nd/^{144}Nd$ value of the Nd Merck standard obtained during the period of measurements was 0.511730 ± 1 (2 σ, n = 12).

Results

Rock units

Rock units identified by integrated petrography and geochemical data are presented here based on field relations, stratigraphy and age analysis (i.e., in the chronological order). The rock names were determined by a combined petrography–geochemistry approach.

Trachyandesite

These are moderately porphyritic samples wherein the feldspar and clinopyroxene phenocrysts are set in a fine-grained groundmass composed essentially of the same minerals (Fig. 3a, b). Rare euhedral amphibole phenocrysts are also present in a few samples. Opaques, apatite and zircon are present as subsidiary phases mainly as micro-phenocrysts or in the groundmass.

Zircons from sample K4-19, a trachyandesite to phonotephrite from the OIB-type series are 37.1–42.5 Ma old with an average of 38.5 Ma (Fig. 4a). Two spots yielded a distinctly younger 14.7 Ma age. This can be explained by sampling from the contact zone with younger magmatic rocks which have a similar mineralogy and texture.

Basalts–andesites

These encompass a wide textural variation from almost vitrophyric volcanic rocks (i.e., lack or include only a few phenocrysts) to microgranular rocks (i.e., contain a fine to medium grained groundmass). The basaltic and andesitic samples are mostly porphyritic with phenocrysts of feldspar (Fsp), clinopyroxene (Cpx), orthopyroxene (Opx), olivine (Ol) and Fe–Ti oxide (Fig. 3c, d). Glass is one of the common constitutes of the rocks groundmass. Feldspar laths, Cpx, Ol, Opx, and opaque microcrystals constitute other components of the groundmass. Feldspar phenocrysts occur as polysynthetic or zoned plagioclase. Cpx is common as augite phenocrysts whereas Ol and Opx only rarely occur. Olivine is represented by pseudomorphs wherein the original mineral has been replaced by secondary chlorite. Orthopyroxene is partly altered but recognizable by its straight extinction and low birefringence colors. In some samples, the proportion and size of microcrystals increase; with texture of these samples approaching microcrystalline rocks (see Online Resource 6a, b for further photomicrographs of these rocks).

Zircons extracted from sample K1-19 from the subalkaline series are 22.1–29.9 Ma old. The zircons form two distinct age clusters, averaging 23.2 Ma and 27.5 Ma (Fig. 4b). Zircons from this sample also yielded two younger spot analyses of 12.7 and 16.0 Ma ages (Online Resource 7). Once again, these can be explained by sampling from the contact with younger magmatic rocks, which have a similar mineralogy and texture.

Analcime basalt–andesite

The presence of analcime in both rocks as phenocrysts and in the groundmass (Fig. 3e–g) is typical of this rock type. Analcime phenocrysts are large (0.5 mm to 5 mm) and poikilitically enclose feldspar and clinopyroxene micro-phenocrysts (Online Resource 6c, d). Feldspar, clinopyroxene and Fe–Ti oxides are also present as phenocrysts. The groundmass is the major constituent of the analcime basalts and andesites and mostly comprises felsic materials (glass, feldspar and analcime). Some Cpx and Fe–Ti oxides are also present in the groundmass. Zircons extracted from sample K3-130, a trachyandesite from the alkaline series, show restricted magmatic ages averaging 24.4 Ma (Fig. 4c).

Amphibole biotite trachyte

These trachytes are weakly porphyritic to almost aphyric samples composed mainly of fine-grained groundmass (Fig. 3h, i). The major phenocryst phase is feldspar, some of which shows polysynthetic twinning. Most feldspars lack twinning or zoning. Clinopyroxene rarely occurs as a microphenocryst phase. Opacitized amphibole and biotite phenocrysts are ubiquitous phases in the trachytes (see Online Resource 6e–h, further photomicrographs of these rocks).

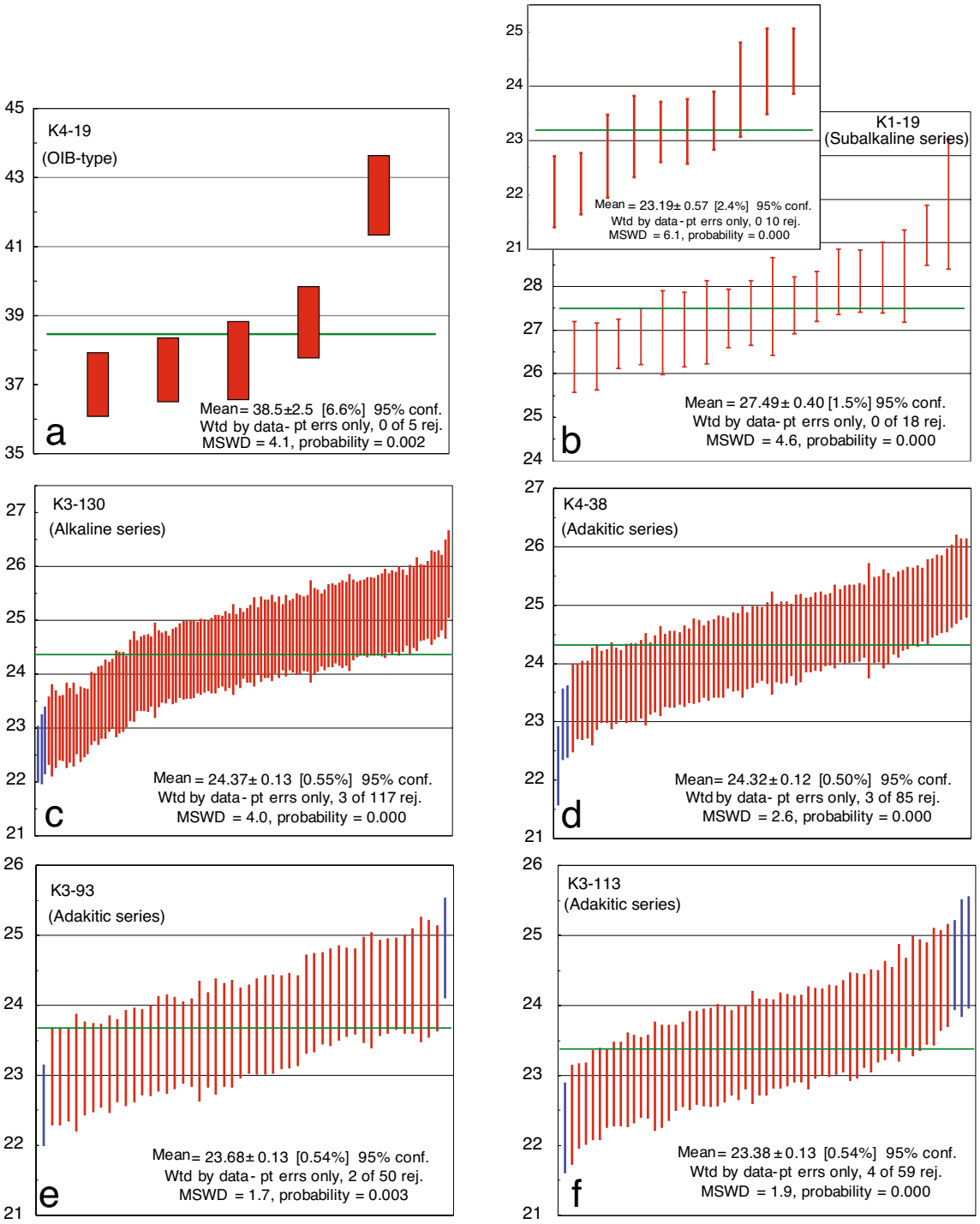

Fig. 4 Zircon U–Pb weighted mean ages obtained from the volcanic rocks of South Kaleybar. These represent the major rock series from the study area

Zircons extracted from samples K4-38, K3-93 and K3-113, from the trachytes (i.e., the adakitic series) show restricted magmatic ages averaging 24.3 Ma, 23.7 Ma and 23.4 Ma, respectively (Fig. 4d–f). The age dated volcanic rocks from across the study area also contain inherited zircons. The inherited zircons span a wide age range from Proterozoic (i.e., 1800 Ma, 700 Ma and 546 Ma), Cambrian (541–539 Ma) Silurian (444–424 Ma), late Devonian—Carboniferous (362–317 Ma), Triassic (223–204 Ma), Jurassic (172–160 Ma) to Cretaceous (108–66 Ma) (see Discussion).

Zircon trace elements

Rare earth element (REE) patterns of the zircons show significant depletion in La, enrichment in heavy rare earth elements (HREE), moderate negative Eu anomalies and positive Ce anomalies (Online Resource 8). These are considered to be magmatic signatures (Belousova et al. 2002; Hanchar and Van Western 2007). No zircon from the study area plotted in the hydrothermal zircon domain on the normalized REE diagrams (Online Resource 8).

Whole-rock major-and trace-element geochemistry

Based on the major-element oxides versus silica (Harker) diagrams, the volcanic rocks from the study area can be classified into two major series; subalkaline and alkaline (Fig. 5). The major-element oxides were recalculated on an anhydrous basis (see Discussion for details). The subalkaline series is characterized by lower K and marginally higher Mg, Fe and Ti as compared to the alkaline series (Fig. 6). The subalkaline series includes a higher number of samples than the alkaline series (i.e., 12 versus 7). However, except for one sample with higher silica, these two series cover almost the same silica range (i.e., 48–58 wt% SiO_2). The subalkaline series contains lower lithophile element (K, Rb, Sr, Ba and Th) abundances and higher high field strength elements (HFSE) and HREE (e.g., Nb, Yb and Y).

Based on the trace-element abundances, some of the intermediate volcanic rocks from the study area show deviations from this bimodal classification. Five samples are exceptionally enriched in REE, especially La and Ce, and HFSE such as Nb (Fig. 6). These are also enriched in lithophile elements and may therefore be called OIB-type series (i.e., the third series from the study area). The trace-element patterns of OIB-type rock series show positive anomalies for Th–U and Pb and negative anomalies for Ba, Ta, Ce, P and Ti (Fig. 7a).

Samples from the subalkaline series show smooth and relatively depleted trace-element patterns (Fig. 7b). More basic members of the subalkaline series show strong negative anomalies for Rb and K, and are alternatively called incompatible element depleted subalkaline basalts. The trace-element patterns of samples from the alkaline series are characterized by very distinctly negative Nb–Ta anomalies. These negative anomalies are more pronounced in the samples with higher alkalis and incompatible elements. The alkaline series rocks are notably depleted in HREE (Fig. 7c) but are not adakites. Only six samples are depleted enough in HREE to be called/considered as adakitic series (i.e., the fourth series from the study area; Figs. 6 and 7d).

Whole-rock Sr–Nd isotopes

Sr and Nd isotopic data obtained from the South Kaleybar region include samples from different compositional affinities (Table 2) as follows; subalkali series rocks (four samples), alkali series rocks (five samples), OIB-type rocks (one sample) and adakitic rocks (three samples). These thirteen samples were selected as they contained the least alteration effects (see Fig. 3e–g and Online Resource 6c–h for photomicrographs of these rocks). The initial $^{87}Sr/^{86}Sr$ and $^{143}Nd/^{144}Nd$ isotopic composition of these samples were calculated based on their ages obtained by zircon U–Pb dating (Fig. 4). The initial Sr isotopic ratios vary from 0.704187 to 0.706048, the initial Nd isotopic ratios vary from 0.512417 to 0.512745, which correspond to initial εNd values of -3.65 and + 2.70, respectively (Fig. 8).

Most volcanic rocks from the study area plot in the mantle array, close to the bulk silica Earth (BSE). The subalkaline series has some of the lowest Sr_i and ε Nd values and plot in the position between the OIB and EMI (i.e., the OIB and EMI array). However, rocks from the alkali series and the adakite series deviate towards significantly higher Sr_i values, approaching the EMI component (Fig. 8).

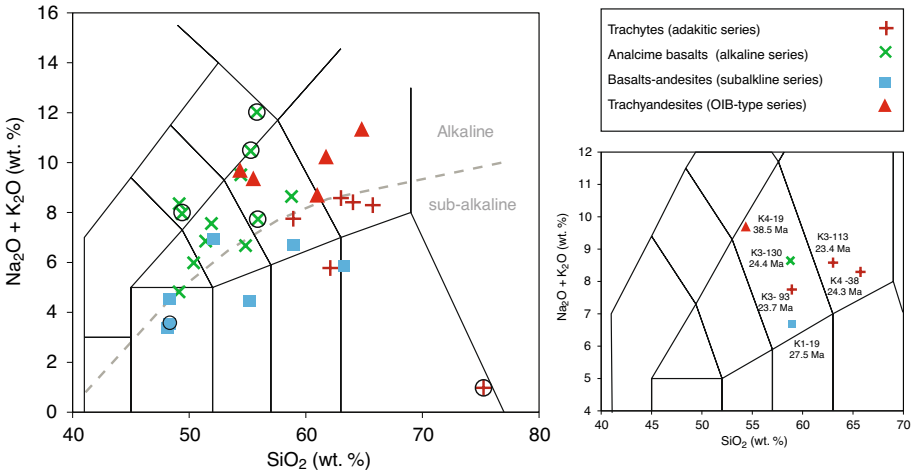

Fig. 5 Total alkalis versus SiO_2 (TAS) plot for South Kaleybar volcanic rocks. The diagram is after Le Bas et al. (1986)

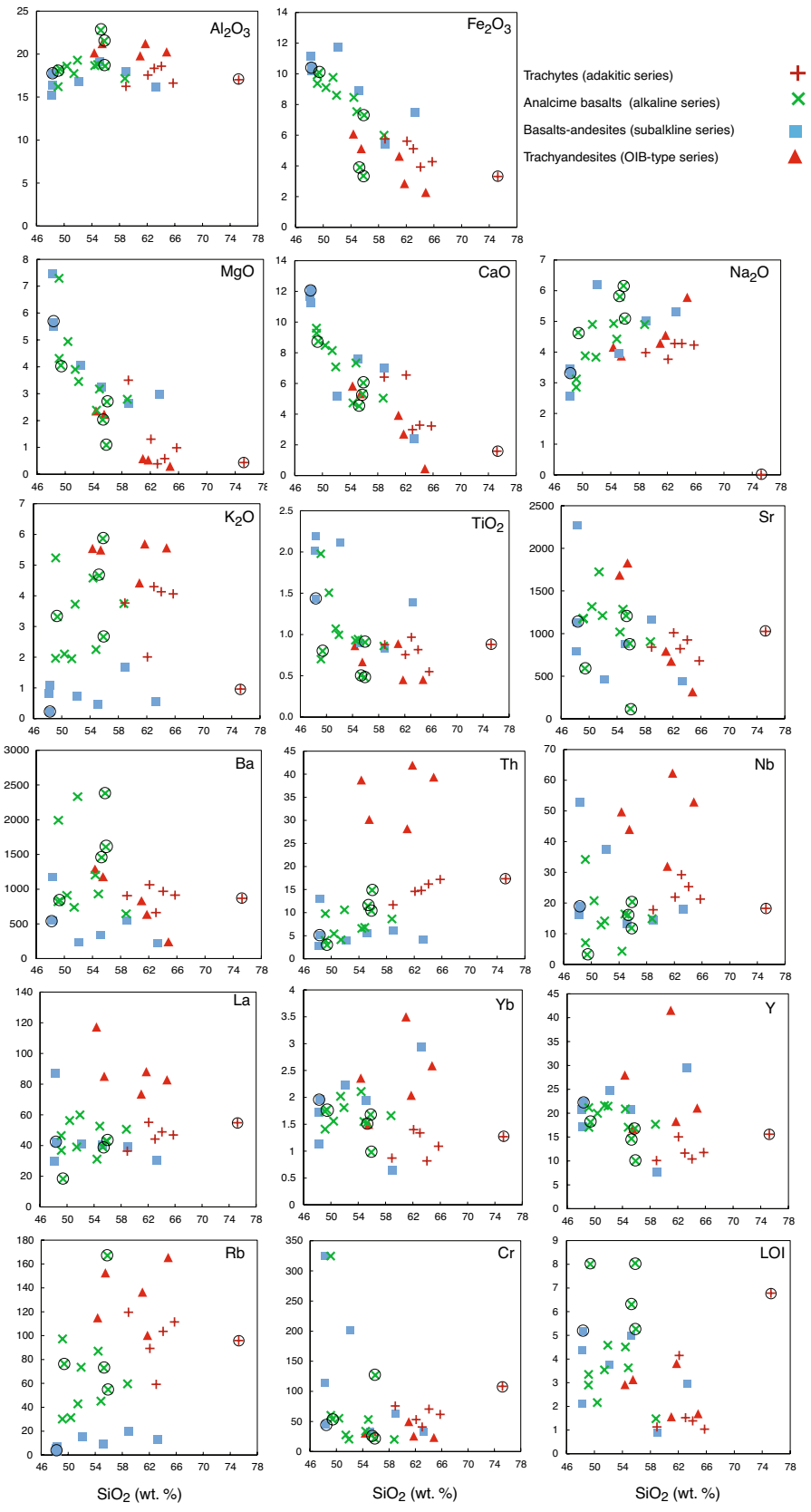

Fig. 6 SiO_2 versus major- and selected trace–element plots for the volcanic rocks from the study area. Encircled samples contain > 5 wt% LOI

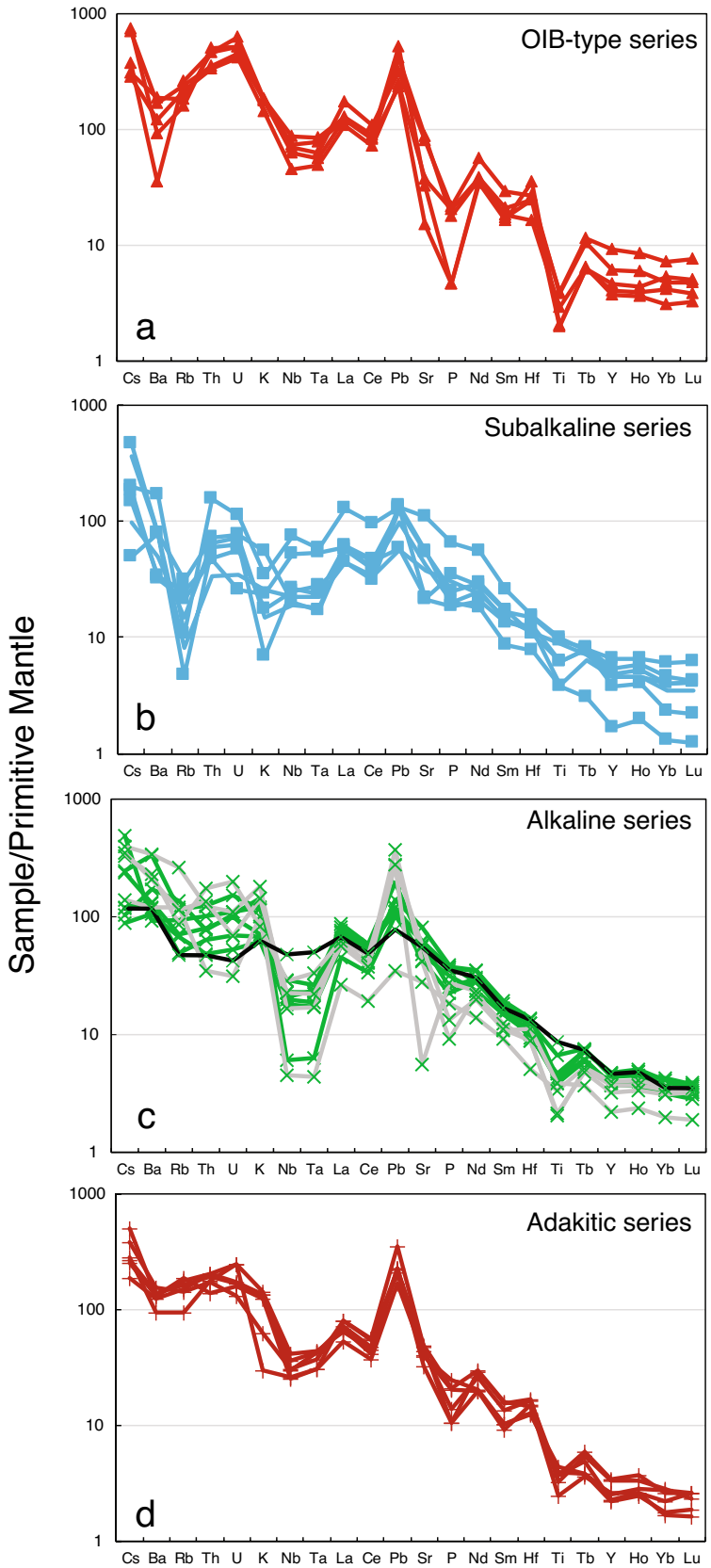

Fig. 7 Primitive-mantle normalized trace–element patterns for the South Kaleybar volcanic rocks. **a** OIB-type series, **b** subalkaline series, **c** alkaline series, and **d** adakite series. Normalizing values are after Sun and Mc Donough (1989). On diagram '**c**' the lease alkaline sample is shown in black and the samples with high LOI (i.e., > 5 wt% LOI) are shown in gray (see Discussionfor details)

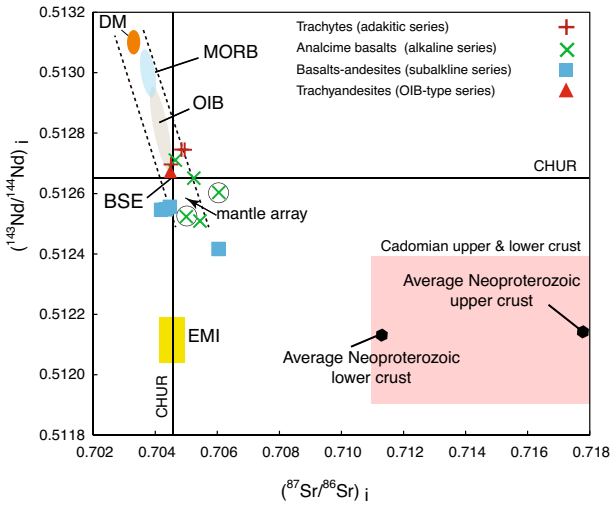

Fig. 8 Initial Sr–Nd isotopic ratios are shown for representative volcanic rocks from South Kaleybar. εNd ($_t$) values are also shown. MORB: mid-ocean ridge basalt; DM: depleted mantle; and OIB: ocean-island basalt are after Zindler and Hart (1986). Data for the Cadomian upper and lower crustal rocks are from Shafaii Moghadam et al. (2015). Encircled samples contain > 5 wt% LOI

Discussion

Alteration and trace-element mobility

The mineralogy and volatile contents are the most prominent measures that determine whether the igneous rocks have maintained their primary magmatic geochemical characteristics or not. The development of secondary minerals in the volcanic rocks from the study area is strictly limited to a few pseudomorphs after primitive Ol and Opx (see petrography). Four samples from the alkaline series with higher LOI contents (i.e., > 5 wt% LOI) show similar trace-element patterns as the other eight samples from this series (i.e., with < 4.58 wt% LOI). This indicates that although a significant portion of the LOI may have been added by alteration, the original compositional signatures of the volcanic rocks have not been significantly modified by post-magmatic processes (e.g., Xie et al. 2018; Yuan et al. 2016). Fundamentally different but coherent trace-element patterns of the South Kaleybar alkaline and subalkaline series rocks, most of which have similar, and relatively high volatile contents (i.e., > 5 wt% LOI), confirms that the primary magmatic signatures are preserved (Polat and Hofmann 2003). The HFSE are considered immobile during post-magmatic alteration and are, therefore, used to monitor element mobility (Pearce et al. 1992). Samples from the study area exhibit a systematic variation of incompatible elements with Nb (Online Resource 9), evidence of the relative immobility of the incompatible elements. This confirms that the volcanic rocks from the study area have preserved their original magmatic geochemical signatures.

Basement of the west Alborz magmatic assemblage

As mentioned above, the volcanic rocks from the study area contain inherited zircons with ages ranging from Proterozoic (1800 Ma) to Cretaceous (66 Ma). The presence of these inherited zircons furnishes proof for substantial crustal contamination in the petrogenesis of the investigated volcanic rocks. The oldest dated crystalline rocks in Iran are typically granitoids and metamorphic rocks that are exposed throughout most parts of Iran including the central Iranian microcontinent, Urumieh–Dokhtar Magmatic Assemblage, Sanandaj–Sirjan and Alborz zones. These rocks provide crystallization ages from the Late Neoproterozoic to Cambrian (Hassanzadeh et al. 2008; Shafaii Moghadam et al. 2018; Sepidbar et al. 2020). Studies conducted on the basement rocks revealed that they contain zircons reworked form older crustal materials (Hassanzadeh et al. 2008). The oldest age yielded from inherited zircons extracted from volcanic rocks of the study area (i.e., 1800 Ma) is younger than the ages of the oldest zircon cores and inherited zircons reported from the basement rocks of Iran (e.g., Nutman et al. 2014; Shakerardakani et al. 2019; Chaharlang and Ghorbani 2019).

OIB-type series (38.5 Ma)

Some mafic-intermediate volcanic rocks from the study area are highly alkaline and enriched in immobile trace elements (e.g., REE and HFSE). One may consider these as representing a rare mafic A-type magmatic rock signature (Azizi et al. 2017; Karsli et al. 2018), particularly so, because they are highly alkaline and contain high abundances of highly incompatible elements (Nb, Ta, Hf and Rb). However, this consideration does not stand close scrutiny most importantly due to: (1) the lack of high Ga/Al ratios; (2) absence of sodic affinity; and (3) lack of any anhydrous compositions (Whalen et al. 1987; Eby and Kochhar 1990). Contrary to the extreme feldspar fractionation that develops high Ga/Al ratios in A-type rocks (Bonin 2007), it appears that instead, clinopyroxene ± feldspar fractionation was responsible for the high Al and K in the OIB-type series from the study area.

Three lines of evidence indicate a dominant asthenospheric mantle source for the OIB-type rocks from the study area. First, the OIB affinity of the trace-element patterns (Fig. 7a). Second, the position of OIB-type rocks from South Kaleybar on the Sr–Nd isotopic ratios diagram wherein they distinctly plot in the mantle array (Fig. 8). Third, the presence of a wide range of inherited zircons in these rocks (i.e., 210–550 Ma; Online Resource 3). The latter also implies the involvement of crustal materials in the magmatic evolution of the OIB-type rocks. However, these rocks show no

significant deviation towards the crustal component on the Sr–Nd isotopic plot (Fig. 8). This might be mainly due to the dominance of Mesozoic ages for the inherited zircons (i.e., the crustal component is not old enough).

The age dated OIB-type rocks from South Kaleybar suggest that the parental asthenospheric mantle melts found their way beneath the study area at 38.5 Ma. The magma batches were limited in volume, trapped in the lower crust, and have mainly undergone fractional crystallization processes to produce the OIB-type melts.

Subalkaline series (27.5 Ma)

The vitrophyric or slightly porphyritic nature of the basic subalkaline rocks from the study area along with their undifferentiated, OIB-type patterns are an important testimony to their rather primitive nature. The absence of negative Nb–Ta anomalies and overall trace-element enrichment suggests that they originated from an asthenospheric mantle.

It is noted that an extensional regime, probably a slab roll-back, at 38.5 Ma (i.e., age of the oldest OIB-type rocks) prompted an asthenospheric mantle upwelling and melting beneath the study area (see above). The asthenospheric magma batches evolved by fractional crystallization to produce the OIB-type melts. However, the influx of asthenospheric mantle melts seems to have increased through time, so that they finally emerged/erupted as subalkaline mafic melts. An extension-induced origin for the South Kaleybar subalkaline (and OIB-type) series is further confirmed by the sedimentary and magmatic records of the regional geology. The development of shallow marine Oligocene deposits, The Lower Red and Qom Formations, across Iran (Vaziri and Sfidari 2012; Karevan et al. 2015) supports the findings of the present study that infers an extensional framework for the Late Eocene to Oligocene magmatism in South Kaleybar. A transition from geochemical signatures of Eocene subduction-related magmatism to Oligocene plume-type magmatic rocks in the neighboring Urumieh–Dokhtar Magmatic Assemblage are regarded as implying a dominant extensional setting in the Late Eocene–Oligocene (Verdel et al. 2011; Ghorbani et al. 2014). A rather wide magmatic age range of 22.1–29.9 Ma (Online Resource 3) for the subalkaline rocks from the study area indicates that this occurred contemporaneously with the alkaline magmatism (i.e., of 24.4 Ma age). In fact, zircon ages from sample K1-19 exhibit a bimodal age distribution with mean ages of 23.2 Ma and 27.5 Ma. The older ages are likely to represent zircons crystallized from the earlier subalkaline melts or they may alternatively be xenocrysts. A similar association of OIB-type and subduction-related alkaline magmatism has been reported from some other magmatic arcs worldwide (Hastie et al. 2011).

Subalkaline volcanic rocks from the study area, however, do not have typical OIB trace-element patterns. A significant depletion in incompatible trace elements that include both mobile and immobile elements Cs and Ta is notable in the subalkaline rocks. Negative anomalies for Rb and K are particularly noticeable. The incompatible trace-element-depleted signature of the subalkaline basalts from the study area is likely to record an earlier partial melting event in their asthenospheric mantle source. Residual amphibole in the mantle source of the subalkaline series helps to explain the K and Rb negative anomalies. The occurrence of OIB-type rocks at 38.5 Ma in the study area with intraplate geochemical signatures (i.e., Fig. 7a) might be the consequence of this earlier partial melting event in the asthenospheric mantle. Samples from the subalkaline series are offset towards less radiogenic Sr isotopic signatures (i.e., towards lower Sr isotopic ratios as compared to the other samples; Fig. 8). This offset is in line with the depleted signature of its mantle source implied by the lithophile element negative anomalies noted on the trace-element patterns of the subalkaline samples. Deviation of one sample from this series towards higher Sr and lower Nd isotopic ratios is regarded as indicating crustal assimilation. This sample with 60.83 wt. % silica is the most differentiated sample from the subalkaline series. It is, therefore, likely to have undergone a larger degree of assimilation fractional crystallization (AFC). The presence of 550 Ma inherited zircons in the subalkaline series rocks from the study area supports contamination by the Cadomian basement rocks.

Two subalkaline rocks from the study area show an adakitic affinity (Fig. 9a, b). One of these (K3-82) does not meet the low-Y requirement of adakites. The rather high Sr content of this sample is likely to be due to the assimilation of some feldspar cumulates. The comparatively high alkaline and lithophile elements in this sample confirm this scenario. The other sample (K1-19) appears to be a genuine adakite (see below; Adakitic series).

Alkaline series (24.4 Ma)

Samples from the alkaline series show strongly negative Nb–Ta anomalies that characterizes typical subduction-related magmatism (White and Patchett 1984; Wilson 1989). The volcanic rocks of alkaline affinity from the study area include a wide compositional range. On the total alkali versus silica diagram, these embrace mildly alkaline to highly alkaline varieties. As the abundances of alkali elements decrease in the alkali series rocks from South Kaleybar, their Nb–Ta abundances increase, so that the trace-element pattern of one sample approaches OIB (i.e., pattern shown in black in Fig. 7c).

Three mechanisms have likely contributed to the compositional spectrum of the South Kaleyber alkaline series

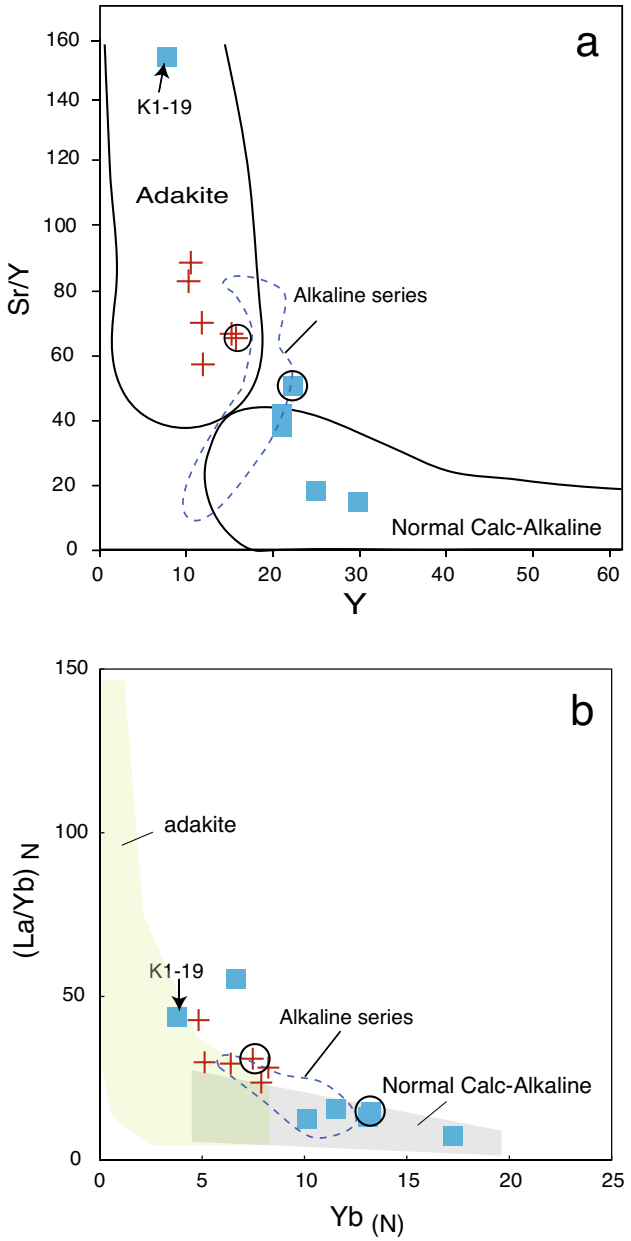

Fig. 9 Adakitic rocks from South Kaleybar are shown on (**a**) Sr/Y versus Y diagram (domains are after Defant et al. (1991); Defant and Drummond (1990) and Martin et al. (2005); **b** $La/Yb_{(N)}$ versus $Yb_{(N)}$ diagram (after Martin 1999)

rocks as follows: (1) Fluid flux: fluids released from the subducting slab are rich in lithophile elements and poor in HFSE, so their contribution to the mantle partial melts increase the LILE/HFSE ratio; (2) Asthenosphere–lithosphere interactions: trace-element patterns of the alkaline series rocks vary between two end-members, one showing negative Nb–Ta anomalies and the other lacking significant negative Nb–Ta anomalies (i.e., they approach the OIB or plume-type pattern). This implies the involvement of two mantle end-members in the evolution of the alkaline series in the study area, lithospheric mantle and asthenospheric mantle, respectively. Asthenosphere–lithosphere interactions are cited as responsible for the wide compositional spectrum of magmatic rocks in arc settings worldwide (e.g., Ma et al. 2013; Deng et al. 2015); (3) Contribution of slab melts: slab partial melts are rich in a wide spectrum of highly incompatible trace elements including LILE and HFSE. This might be the reason as to why the samples from South Kaleybar alkaline series rocks plot near the adakitic domain on the Sr/Y versus Y plot (Fig. 9a, b).

Samples from the alkaline series are mostly nepheline normative (Table 1). The alkaline series samples that plot in the highly alkaline domain on the TAS diagram (i.e., tephrite, tephrite basanite, phonotephrite, tephriphonolite) contain large analcime phenocrysts, whereas those that plot in the mid-alkaline domain on the TAS diagram (i.e., trachybasalt, trachyandesite) lack analcime. Whether analcime occurs as a primary or secondary mineral is highly controversial (Deer et al. 2013). The following three reasons suggest a primary origin for analcime present in the South Kaleybar volcanic rocks: (1) no case of analcime replacing former minerals has been observed; (2) the analcime crystals are euhedral in shape; and (3) some analcime embraces concentric zoned feldspar and clinopyroxene crystals (Fig. 3). However, it is widely believed that analcime usually replaces former primary minerals such as leucite and nepheline as a result of alteration or subsolidus reactions (Gupta and Fyfe 1975; Wilkinson 1977). It is noted above (see the Alteration and trace-element mobility) that the highly alkaline samples maintained their primitive geochemical characteristics. These along with the strongly negative Nb–Ta anomalies for the trace-element patterns of the highly alkaline rocks indicate a typical metasomatized lithospheric mantle source. Alternatively, hydrous melting of metasomatized asthenosphere above the slab could be the source region. Particularly, because of the higher temperature in the asthenosphere that makes partial melting more likely to occur. However, due to the strongly depleted Nb–Ta signature of the alkaline series the involvement of the lithospheric mantle is inevitable.

The alkaline series covers a significant area across the mantle array on the Sr–Nd isotopic plot. This likely implies mantle end-member interactions. Deviation of the alkaline series rocks data points towards higher Sr and lower Nd isotopic ratios (Fig. 8) might alternatively be regarded as indicating assimilation of crustal rocks. Additionally, the presence of 550-Ma-old inherited zircons in the alkaline series rocks (Online Resource 3) from the study area supports contamination by the Cadomian basement rocks.

Adakitic series (24.3–23.4 Ma)

These rocks plot in the trachyandesite and trachyte fields. They are characterized by rather low Y and HREE and higher Sr and LREE as compared to the normal calc-alkaline igneous rocks so that they plot in the adakite field (Fig. 9a–b). Most adakites plot in the dacite and rhyolite fields; however, some adakites show trachytic compositions (Azizi et al. 2014; Ji et al. 2021; Khalatbari et al. 2020). Adakites were initially defined as the product of partial melting of subducted young, hot, flat oceanic slabs (Defant and Drummond 1990). Martin et al. (2005) classified the adakites into high silica (HSA) and low silica (LSA) varieties. The HSA were considered to represent melts of subducted oceanic crust that have reacted with mantle peridotites as they ascended through the mantle wedge. The LSA were interpreted to have formed by partial melting of mantle wedge peridotites whose composition were modified by reaction with slab-derived melts. The LSA and HSA share a sodic affinity but are distinguished from each other by lower SiO_2, higher MgO and $CaO + Na_2O$ contents for the LSA, compared to high HSA. The adakitic samples from South of Kaleybar differ from both HSA and LSA by having higher K_2O. K_2O/Na_2O ratios for these rocks are ~1, while the corresponding ratio for the oceanic slab-related adakites is ~0.42 (Martin et al. 2005). Moreover by having a rather enriched isotopic signature ($Sr_i = 0.704506$—0.704951), these rocks are distinct from slab-derived adakites (typically < 0.7040). High-K adakitic rocks (also known as C-type or potassic adakites) are believed to be generated by different petrogenetic processes such as (1) high-pressure fractional crystallization from a mafic melt derived from mantle wedge peridotites (e.g., Macpherson et al. 2006; Li et al. 2013; Ribeiro et al. 2016); (2) melting of thickened mafic lower crust underplated by hot basic magmas (e.g., Zhang et al. 2001; Hou et al. 2004); (3) melting of delaminated lower crust (e.g., Xiao and Clemens 2007; Xu et al. 2002). It has been proven than fractionation of amphibole from parental basaltic magmas could efficiently deplete the melts in HREE and Y and elevate their Sr/Y ratio producing the adakitic signature (Davidson et al. 2007; Du et al. 2017). Despite the presence of amphibole phenocrysts in the adakites from South Kaleybar, an amphibole-dominated fractional crystallization model for their petrogenesis is not supported by the Dy/Yb versus SiO_2 diagram (not shown). Moreover, the lack of correlation between the Sr/Y ratio and SiO_2 content in the adakites rules out such a scenario. In addition, high Cr and Ni contents of the adakites argues against their generation by extensive fractional crystallization from a non-adakitic parental melt.

Involvement of the continental crust in genesis of the adakites from South Kaleybar is indicated by the presence of inherited zircons. However, some trace and geochemical characteristics of the adakites are not in line with a crustal origin. As mentioned above, adakites in the present study exhibit high Cr and Ni contents (40.94–108.1 and 11.57–83.2 ppm, respectively). These high abundances of compatible trace elements are inconsistent with those of lower crust partial melts (e.g., Deng et al. 2018). On the Sr–Nd isotopic plot, the samples do not fall in the crustal-derived melts domain but instead, their Sr–Nd ratios suggest a mantle origin. One adakitic rock plots in the mantle array. The two other adakites show higher initial $^{87}Sr/^{86}Sr$ ratios. The isotopic data can best be explained by a binary mixture of two isotopically distinct sources (i.e., crustal and mantle sources). The high content of compatible trace elements and the presence of inherited zircons also confirms this model for adakites from South Kaleybar.

Considering a significant contribution by the asthenospheric mantle to the magmatism in the study area, it is likely that asthenospheric ascent prompted thermal erosion of the overlying lithosphere and led to the delamination of eclogitic lower continental crust. Detachment and sinking of the lower crust slivers into the mantle led to the generation of hybrid adakitic melts that interacted with the mantle. The melts en route to the surface were probably contaminated by the Cadomian basement and captured inherited zircons.

One subalkaline intermediate rock (K1-19) from the study area shows an adakitic affinity. This sample plots close to the boundary between the high-silica adakite and low-silica adakite fields. Low-silica adakites are regarded as the product of a mantle metasomatized by slab melts. The rolled-back slab might have locally ruptured to furnish limited slab melt that ascended along with and reacted with the rising asthenospheric melt.

Conclusions

The present study provides a detailed account of the origin and petrogenesis of Tertiary volcanic rocks from South Kaleybar and classifies these into four major series: I—intermediate (alkaline) OIB-type series, II—mafic to intermediate subalkaline series, III—mafic alkaline series, and IV—intermediate adakitic series. Listed below are the major findings of the present study.

1- Anorogenic, asthenospheric mantle contribution to the South Kaleybar magmatism is implied by the presence of both 38.5 Ma intermediate OIB-type rocks and

27.5 Ma subalkaline rocks. On the other hand, subduction related inputs, dominantly metasomatized lithospheric mantle (± asthenospheric mantle) contribution to the magmatism is indicated by the 24.4 Ma alkaline affinity rocks along with 24.3 Ma–23.4 Ma adakitic volcanism.

2 –38.5-Ma-old OIB-type rocks indicate the partial melting of an asthenospheric mantle influx beneath the study area that was triggered by a slab rollback due to an anorogenic (i.e., extensional) setting (Fig. 10). The partial melt underwent Cpx ± Fsp fractionation.

3 –27.5-Ma-old subalkaline mafic volcanic rocks from South Kaleybar, bear a plume-type asthenospheric mantle signature, and plot in the OIB-EMI array on the Sr–Nd isotope diagram. The highly incompatible element depleted signature of the subalkaline series probably developed as a consequence of former derivation of OIB-type partial melts in the Eocene (38.5 Ma). Other incompatible trace elements are not depleted to the same extent as Rb and K. This is likely due to the presence of residual amphibole in the mantle source.

4- The OIB-type series rocks contain some inherited zircons that have been incorporated when their melts ascended through the Cadomian crust.

5 –24.4-Ma-old alkaline (i.e., highly to mid-alkaline) mafic volcanic rocks from South Kaleybar are suggested to have been derived mainly from the metasomatized lithospheric mantle as suggested by their negative Nb–Ta anomalies, which have undergone some degrees of interaction with the asthenospheric mantle (Fig. 10).

6 –24.3–23.4-Ma-old adakitic rocks from the study area show high K/Na and low Ca/Al ratios, signatures of extension-induced delaminated crustal partial melts. Rather high compatible elements in the adakites and adakitic affinity of one subalkaline intermediate rock from South Kaleybar indicate that the partial melts of delaminated crustal rocks were exposed to and reacted with the asthenospheric melt.

7- Deviation of Sr–Nd isotopic data points towards higher Sr and lower Nd isotopic ratios in the alkaline and adakite series rocks indicate that their parental melts have undergone crustal contamination. Inherited zircons of 540 Ma age found in these rocks support the contamination by Cadomian crustal materials.

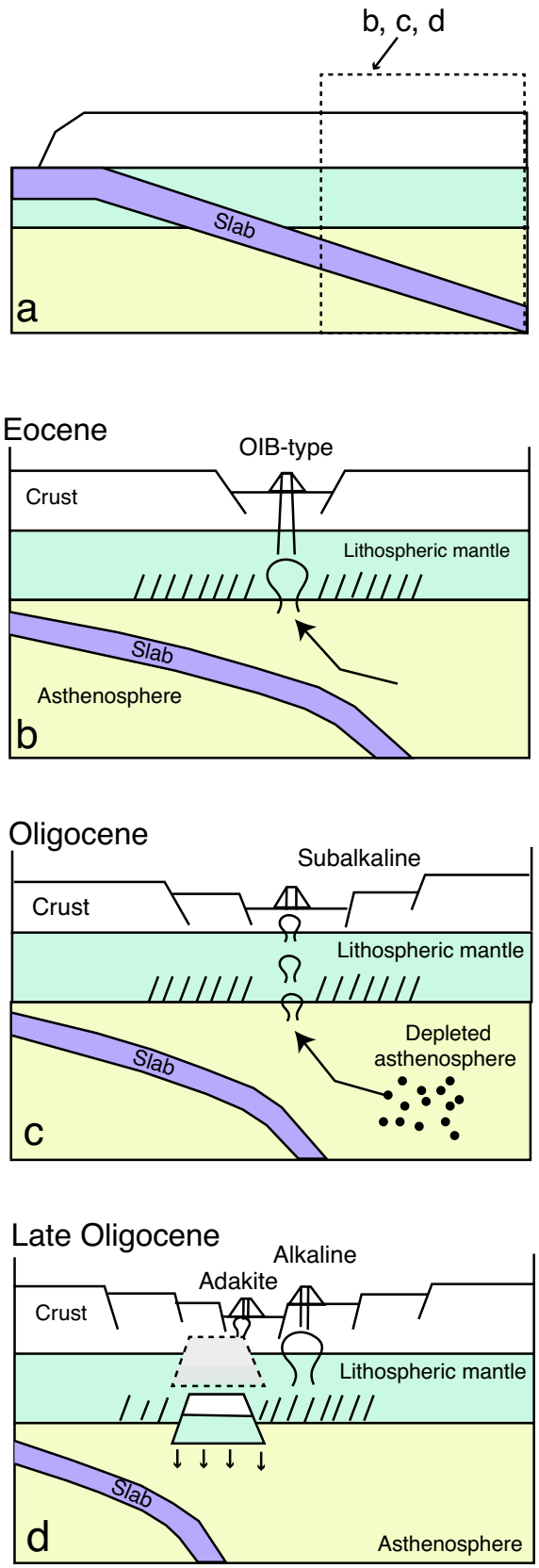

Fig. 10 Geodynamic model summarizing the South Kaleybar magmatic compositional evolution through time

Supplementary Information The online version contains supplementary material available at https://doi.org/10.1007/s00531-023-02313-6.

Acknowledgements This work is derived from the Ph.D. thesis of Mohammad Paydari (2023). TMU, ETH and UC Santa Barbara are acknowledged for their funds and facilities. Two anonymous reviewers and Dr. Lin Sutherland are acknowledge for their comments which significantly improved this manuscript. Chief Editor Prof. Ulrich Riller and the Topic Editor are also acknowledged for their valuable comments and editorial handling which greatly improved this manuscript. Dr Mir A.A. Mokhtari is sincerely acknowledged for his advice while in the field. The Songun Copper Mining Complex is sincerely appreciated for furnishing the field camp during field work. The staff and students of the Geology Department from TMU are acknowledged for their friendship and support.

Data availability The authors confirm that the data supporting the findings of this study are available within the article and its supplementary materials.

References

Aghazadeh M, Castro A, Rashidnejad Omran N, Emami MH, Moinvaziri H, Badrzadeh Z (2010) The gabbro (shoshonitic)-monzonite-granodiorite association of Khankandi pluton, Alborz Mountains, NW Iran. J Asian Earth Sci 38:199–219

Aghazadeh M, Castro A, Badrzadeh Z, Vogts K (2011) Post-collisional polycyclic plutonism from the Zagros hinterland: the Shaivar Dagh plutonic complex, Alborz belt. Iran Geol Mag 148:980–1008

Ahmadvand A, Ghorbani MR, Mokhtari MAA, Chen Y, Amidon W, Santos JF, Paydari M (2021) Lithospheric mantle, asthenosphere, slab and crustal contribution to petrogenesis of Eocene to Miocene volcanic rocks from the west Alborz magmatic assemblage, SE Ahar. Iran Geol Mag 158:375–406

Alavi M (1996) Tectonostratigraphic synthesis and structural style of the Alborz mountain system in northern Iran. J Geodynamics 21:1–33

Asiabanha A, Foden J (2012) Post-collisional transition from an extensional volcanosedimentary basin to a continental arc in the Alborz Ranges, N-Iran. Lithos 148:98–111

Azizi H, Asahara Y, Tsuboi M, Takemura K, Razyani S (2014) The role of heterogenetic mantle in the genesis of adakites northeast of Sanandaj, northwestern Iran. Geochemistry 74:87–97

Azizi H, Kazemi T, Asahara T (2017) A-type granitoid in Hasansalaran complex, northwestern Iran: evidence for extensional tectonic regime in northern Gondwana in the late paleozoic. J Geodyn 108:56–72

Babazadeh S, Ghorbani MR, Brocker M, Antonio MD, Cottle J, Gebbing T, Mazzeo FC, Ahmadi P (2017) Late Oligocene-Miocene mantle upwelling and interaction inferred from mantle signatures in gabbroic to granitic rocks from the Urumieh-Dokhtar arc, south Ardestan. Iran Inter Geol Rev 59:1590–1608

Belousova EA, Griffin WL, O'Reilly SY, Fisher NJ (2002) Igneous zircon: trace element composition as an indicator of source rock type. Contrib Miner Petrol 143:602–622

Berberian F, Berberian M (1981) Tectono-plutonic episodes in Iran. In: Gupta HK, Delany FM (eds) Zagros-Hindu Kush-Himalaya geodynamic evolution. AGU, Washington D.C., pp 5–32

Black LP, Kamo SL, Allen CM, Davis DW, Aleinikoff JN, Valley JW, Mundil R, Campbell IH, Korsch RJ, Williams IS, Foudoulis C (2004) Improved $^{206}Pb/^{238}U$ microprobe geochronology by the monitoring of a trace-element-related matrix effect; SHRIMP, ID–TIMS, ELA–ICP–MS and oxygen isotope documentation for a series of zircon standards. Chem Geol 205:115–140

Bonin B (2007) A-type granites and related rocks: evolution of a concept, problems and prospects. Lithos 97:1–29

Castro M, Aghazadeh M, Badrzadeh Z, Chichorro M (2013) Late Eocene-Oligocene post-collisional monzonitic intrusions from the Alborz magmatic belt, NW Iran. An example of monzonite magma generation from a metasomatized mantle source. Lithos 180–181:109–127

Chaharlang R, Ghorbani MR (2019) A hidden crust beneath the central Urumieh-Dokhtar magmatic arc revealed by inherited zircon ages, Tafresh. Iran Geol J 55:3770–3781

Chiu HY, Chung SL, Zarrinkoub MH, Pang KN, Lee HY (2018) Cadomian basement evolution and Cenozoic crustal growth in Iran: constraints from zircon Hf isotopes. AGU, Washington D.C.

Cottle JM, Waters DJ, Riley D, Beyssac O, Jessup MJ (2011) Metamorphic history of the South Tibetan detachment system, Mt. Everest region, revealed by RSCM thermometry and phase equilibria modelling. J Metamorph Geol 29(5):561–582. https://doi.org/10.1111/jmg.2011.29

Cottle JM, Burrows AJ, Kylander-Clark A, Freedman PA, Cohen RS (2013) Enhanced sensitivity in laser ablation multi-collector inductively coupled plasma mass spectrometry. J Anal Atom Spectrom 28:1700–1706. https://doi.org/10.1039/c3ja50216c

Davidson J, Turner S, Handley H, Macpherson C, Dosseto A (2007) Amphibole "sponge" in arc crust? Geology 35:787–790

Deer WA, Howie RA, Zussman J (2013) An Introduction to the Rock-Forming Minerals. Mineralogical Society of Great Britain and Ireland, London, p 498

Defant MJ, Drummond MS (1990) Derivation of some modern arc magmas by melting of young subducted lithosphere. Nature 347:662–665

Defant MJ, Richerson PM, De Boer JZ, Stewart RH, Maury RC, Bellon H, Drummond MS, Feigenson MD, Maury RC, Jackson TE (1991) Dacite genesis via both slab melting and differentiation: petrogenesis of La Yeguada volcanic complex, Panama. J Petrol 32:1101–1142

Deng Y-F, Song X-Y, Hollings P, Zhou T, Yuan F, Chen L-M, Zhang D (2015) Role of asthenosphere and lithosphere in the genesis of the early Permian Huangshan mafic–ultramafic intrusion in the Northern Tianshan, NW China. Lithos 227:241–254

Deng C, Sun G, Sun D, Huang H, Zhang J, Gou J (2018) Origin of C type adakite magmas in the NE Xing'an block, NE China and tectonic implication. Acta Geochim 37:281–294

Du JG, Du YS, CaO Y (2017) Important role of hornblende fractionation in generating the adakitic magmas in Tongling, Eastern China: evidence from amphibole megacryst and cumulate xenoliths and host gabbros. Int Geol Rev 60:1381–1403

Eby GN, Kochhar N (1990) Geochemistry and petrogenesis of the Malani Igneous Suite, North Peninsular India. J Geol Soc India 36:109–130

Emami MH (2000) 1:100000 Geologic Map of Kaleybar, Iran. Tehran. Geol Survey Iran, map no:5467

Ghorbani MR (2006) Lead enrichment in Neotethyan volcanic rocks from Iran: the implications of a descending slab. Geochem J 40:557–568

Ghorbani MR, Bezenjani RN (2011) Slab partial melts from the metasomatizing agent to adakite, Tafresh, Eocene volcanic rocks. Iran Island Arc 20:188–202

Ghorbani MR, Graham IT, Ghaderi M (2014) Oligocene—Miocene geodynamic evolution of the central part of Urumieh-Dokhtar Arc of Iran. Int Geol Rev 56(8):1039–1050

Guillong M, Meier DL, Allan MM, Heinrich CA, Yardley BW (2008) Appendix A6: SILLS: A MATLAB-based program for the

reduction of laser ablation ICP-MS data of homogeneous materials and inclusions. MAC Short Course 40:328–333
Gupta AK, Fyfe WS (1975) Leucite survival: the alteration to analcime. Can Mineral 13:361–363
Hanchar JM, Miller CF (1993) Zircon zonation patterns as revealed by cathodoluminescence and backscattered electron images: Implications for interpretation of complex crustal histories. Chem Geol 110:1–13
Hanchar JM, Rudnick RL (1995) Revealing hidden structures: The application of cathodoluminescence and back-scattered electron imaging to dating zircons from lower crustal xenoliths. Lithos 36:289–303
Hanchar JM, van Wetrenen W (2007) Rare earth element behavior in zircon–melt systems. Elements 3:37–42
Hassanzadeh J, Stockli DF, Horton BK, Axen GJ, Stockli LD, Grove M, Schmitt AK, Walker JD (2008) U-Pb zircon geochronology of late Neoproterozoic-early Cambrian granitoids in Iran: Implications for paleogeography, magmatism, and exhumation history of Iranian basement. Tectonophysics 451:71–96
Hastie AR, Mitchell SF, Kerr AC, Minifie MJ, Millar IL (2011) Geochemistry of rare high- Nb basalt lavas: are they derived from a mantle wedge metasomatised by slab melts? Geochim Cosmochim Acta 75:5049–5072
Horstwood MS, Kosler J, Gehrels G, Jackson SE, McLean NM, Paton C, Pearson NJ, Sircombe K, Sylvester P, Vermeesch P (2016) Community-derived standards for LA-ICP-MS U-(Th-) Pb geochronology-uncertainty propagation, age interpretation and data reporting. Geostand Geoanalitical Res 40:311–332
Hoskin PWO (2005) Trace-element composition of hydrothermal zircon and the alteration of Hadean zircon from the Jack Hills, Australia. GCA 69:637–648
Hou ZQ, Gao YF, Qu XM, Rui ZY, Mo XX (2004) Origin of adakitic intrusives generated during mid-Miocene east–west extension in southern Tibet. Earth Planet Sci Lett 220:139–155
Jackson SE, Pearson NJ, Griffin WL, Belousova EA (2004) The application of laser ablation-inductively coupled plasma-mass spectrometry to in situ U-Pb zircon geochronology. Chem Geol 211:47–69
Jaffey AH, Flynn KF, Glendenin LE, Bentley WC, Essling AM (1971) Precision Measurement of half-lives and specific activities of ^{235}U and ^{238}U. Phys Rev C 4:1889–1906
Jahangiri A (2007) Post-collisional Miocene adakitic volcanism in NW Iran: geochemical and geodynamic implications. J Asian Earth Sci 30:433–447. https://doi.org/10.1016/j.jseaes.2006.11.008
Ji C, Yan LL, Lu L, Jin X, Huang Q, Zhang KJ (2021) Anduo late cretaceous high-K calc-alkaline and shoshonitic volcanic rocks in central Tibet, western China: relamination of the subducted Meso-Tethyan oceanic plateau. Lithos 400–401:106345
Karevan M, Vaziri-Moghaddam H, Mahboubi A, Moussavi-Harami R (2015) Biostratigraphy and paleo-ecological reconstruction on Scleractinian reef corals of Rupelian-Chattian succession (Qom formation) in northeast of Delijan area. Geopersia 4(1):11–24
Karsli O, Aydin F, Uysal I, Dokuz A, Kumral M, Kandemir R, Budakoglu M, Ketenci M (2018) Latest Cretaceous "A2-type" granites in the Sakarya Zone, NE Turkey: partial melting of mafic lower crust in response to roll-back of Neo-Tethyan oceanic lithosphere. Lithos 302–303:321–328
Khalatbari Jafari M, Salehi Siavashani N, Babaie HA, Xiao W, Faridi M, Ao S (2020) Late Cenozoic volcanism in the Almaludag region, Azerbaijan province, northwest Iran: evidence for post-collisional extension. J Geody 141–142:101779
Koschek G (1993) Origin and significance of the SEM cathodoluminescence from zircon. J Microsc 171:223–232
Kylander-Clark ARC, Hacker BR, Cottle JM (2013) Laser ablation split-stream ICP petrochronology. Chem Geol 345:99–112. https://doi.org/10.1016/j.chemgeo.2013.02.019
Le Bas MJ, Le Maitre RW, Streckeisen A, Zanettin B (1986) A chemical classification of volcanic rocks based on the total alkali–silica diagram. J Petrol 27:445–450
Lechmann A, Burg JP, Ulmer P, Guillong M, Faridi M (2018) Metasomatized mantle as the source of mid-Miocene-quaternary volcanism in NW-Iranian Azerbaijan: geochronological and geochemical evidence. Lithos 304–307:311–328
Li XH, Li ZX, Li WX, Wang XC, Gao Y (2013) Revisiting the "C-type adakites" of the Lower Yangtze River Belt, central eastern China: in-situ zircon Hf–O isotope and geochemical constraints. Chem Geol 345:1–15
Ludwig KR (2012) Isoplot 3.75: a geochronological toolkit for Microsoft Excel, Spec. Publ., no. 5. Berkeley Geochronology Center, Berkeley, p 75p
Ma L, Wang Q, Li Z-X, Wyman DA, Jiang Z-Q, Yang J-H, Gou G-N, Guo H-F (2013) Early late Cretaceous (ca. 93 Ma) norites and hornblendites in the Milin area, eastern Gangdese: lithosphere–asthenosphere interaction during slab roll-back and an insight into early late Cretaceous (ca. 100–80 Ma) magmatic "flare-up" in southern Lhasa (Tibet). Lithos 172–173:17–30
Macpherson CG, Dreher ST, Thirlwall MF (2006) Adakites without slab melting: High pressure differentiation of island arc magma, Mindanao, the Philippines. Earth Planet Sci Lett 243(3–4):581–593
Martin H (1999) Adakitic magmas: modern analogues of Archaean granitoids. Lithos 46:411–429
Martin H, Smithies RH, Rapp R, Moyen JF, Charnpion D (2005) An overview of adakite, tonalite-trondbjcmitc-granodiorite (TTG) and sanukitoid: relationships and some implications for crustal evolution. Lithos 79:1–24
McKinney ST, Cottle, JM, Lederer GW (2015) Evaluating rare earth element (REE) mineralization mechanisms in Proterozoic gneiss, Music Valley, California. GSA Bulletin 127(7–8):1135–1152. https://doi.org/10.1130/B31165.1
Moinvaziri H (1985) Volcanisme tertiaire et quaternaire en Iran. These d'Etat Université Paris-Sud, Orsay, p 278
Nabatian G, Ghaderi M, Neubauer F, Honarmand M, Lui X, Dong Y, Jiang SY, Bernroider M (2014) Petrogenesis of Tarom high-potassic granitoids in the Alborz–Azarbaijan belt, Iran: geochemical, U-Pb zircon and Sr–Nd–Pb isotopic constraints. Lithos 184–187:324–345
Nutman A, Mohajjel M, Bennett V, Fergusson CL (2014) Gondwanan Eoarchean-Neoproterozoic ancient crustal material in Iran and Turkey: zircon U-Pb–Hf isotopic evidence. Can J Earth Sci 51:272–285
Omrani J, Agard P, Whitechurch H, Benoit M, Prouteau G, Jolivet L (2008) Arc magmatism and subduction history beneath the Zagros Mountains, Iran: a new report of adakites and geodynamic consequences. Lithos 106:380–398
Paton C, Woodhead JD, Hellstrom JC, Hergt JM, Greig A, Maas R (2010) Improved laser ablation U-Pb zircon geochronology through robust downhole fractionation correction. Geochem Geophy Geosys (G3) 11:Q0AA06
Paton C, Hellstrom J, Paul B, Woodhead J, Hergt J (2011) Iolite: Freeware for the visualisation and processing of mass spectrometric data. J Anal Spectrom 26:2508–2518
Paydari M (2023) Petrology and geochemistry of Tertiary volcanic rocks from South Kaleybar. Ph.D thesis, Tarbiat Modares University (in Persian), 120 p
Pearce JA, Thirlwall MF, Ingram G, Murton BJ, Arculus RJ, Van Der Laan SR (1992) Isotopic evidence for the origin of boninites and related rocks drilled in the Izu-Bonin (Ogasawara) forearc, LEG 1251. Proc Ocean Drill Prog Sci Results 125:237–261

Petrus JA, Kamber BS (2012) VizualAge: a novel approach to laser ablation ICP-MS U-Pb geochronology data reduction. Geostand Geoanalytical Res 36:247–270

Pin C, Briot D, Bassin C, Poitrasson F (1994) Concomitant separation of strontium and samarium-neodymium for isotopic analysis in silicate samples, based on specific extraction chromatography. Anal Chim Acta 298:209–217

Polat A, Hofmann A (2003) Alteration and geochemical patterns in the 3.7–3.8 Ga Isua greenstone belt, West Greenland. Precamb Res 126:197–218

Rabiee A, Rossetti F, Asahara Y, Azizi H, Lucci F, Lustrino M, Nozaem R (2020) Long-Lived, Eocene-Miocene stationary magmatism in NW Iran along a transform plate boundary. Gondw Res 85:237–262

Ribeiro JM, Maury RC, Grégoire M (2016) Are adakites slab melts or high-pressure fractionated mantle melts? J Petrol 57(5):839–862

Rolland Y (2017) Caucasus collisional history: review of data from East Anatolia to West Iran. Gondw Res 49:130–146

Sepidbar F, Shafaii Moghadam H, Li C, Stern RJ, Jiantang P, Vesali Y (2020) Cadomian magmatic rocks from Zarand (SE Iran) formed in a retro-arc basin. Lithos 366:105569

Shad Manaman N, Shomali H, Koyi H (2011) New constraints on upper-mantle S-velocity structure and crustal thickness of the Iranian plateau using partitioned waveform inversion. Geophys J Int 184:247–267

Shafaii Moghadam H, Khademi M, Hu Z, Stern RJ, Santos JF, Wu Y (2015) Cadomian (Ediacaran–Cambrian) arc magmatism in the ChahJam–Biarjmand metamorphic complex (Iran): magmatism along the northern active margin of Gondwana. Gondw Res 27:439–452

Shafaii Moghdam H, Griffin WL, Li XH, Santos JF, Karsli O, Stern RJ, Ghorbani G, Gain S, Murphy R, O'Reilly (2018) Crustal evolution of NW Iran: Cadomian Arcs, archean fragments and the Cenozoic magmatic flare-up. J Petrol 58:2143–2190

Shakerardakani F, Li XH, Ling XX, Li J, Tang GQ, Liu Y, Monfared B (2019) Evidence for Archean crust in Iran provided by ca 2.7 Ga zircon xenocrysts within amphibolites from the Sanandaj-Sirjan zone, Zagros orogeny. Percamberian Res 332:105390

Slama J, Kosler J, Condon DJ, Crowley JL, Gerdes A, Hanchar JM, Horstwood M, Morris GA, Nasdala L, Norberg N, Schaltegger U, Schoene B, Tubrett MN, Whitehous M (2008) Plesovice zircon—a new natural reference material for U-Pb and Hf isotopic microanalysis. Chem Geol 249:1–35

Stacey JS, Kramers JD (1975) Approximation of terrestrial lead isotope evolution by a two-stage model. Earth Planet Sci Lett 26(2):207–221. https://doi.org/10.1016/0012-821X-(75)90088-6

Steiger RH, Jäger E (1977) Subcommission on geochronology: convention on the use of decay constants in geo and cosmochronology. Earth Planet Sci Lett 36(3):359–362. https://doi.org/10.1016/0012-821X(77)90060-7

Sun SS, Mc Donough WF (1989) Chemical and isotopic systematics of oceanic basalts: implications for mantle composition and processes. In: Saunders AD, Norry MJ (eds) Magmatism in the Ocean Basins. Geol Soc Lond, Spec Publ no. 42, London, pp 313–345

Vaziri MR, Sfidari E (2012) The Tethyan seaway Iranian plate Oligo-Miocene deposits (the Qom formation): distribution of Rupelian (early Oligocene) and evaporate deposits as evidences for timing and trending of opening and closure of the Tethyan seaway. Carbonate Evaporite 28:321–345

Verdel C, Wernicke BP, Hassanzadeh J, Guest B (2011) A Paleogene extensional arc flare-up in Iran. Tectonics 30:TC3008

Vermeesch P (2018) IsoplotR: a free and open toolbox for geochronology. Geosci Front 9:1479–1493

Vermeesch P (2021) On the treatment of discordant detrital zircon U-Pb data. Gchron 3:247–257

Von Quadt A, Gunther D, Frischknecht R, Dietrich V (1999) Minor and trace element determinations in Li2B407 fused USGS standard materials calibrated without matrix-matched standards using laser ablation ICP-MS. J Conf Abst 4:819

Von Quadt A, Wotzlaw JF, Buret Y, Large SJ, Peytcheva I, Trinquier A (2016) High-precision zircon U/Pb geochronology by ID-TIMS using new 10^{13} ohm resistors. J Anal at Spectrom 31:658–665

Whalen JB, Currie KL, Chappell BW (1987) A-type granites: geochemical characteristics, discrimination and petrogenesis. Contrib Mineral Petrol 95:407–419

White WM, Patchett J (1984) Hf-Nd-Sr isotopes and incompatible element abundances in island arcs: implications for magma origins and crust-mantle evolution. Earth Planet Sci Lett 67:167–185

Wiedenbeck M, Alle P, Corfu F, Griffin WL, Meier M, Oberli F, Von Quadt A, Roddick JC, Spiegel W (1995) Three natural zircon standards for U-Th-Pb, Lu-Hf, trace-element and REE analyses. Geostand Newslett 19:1–23. https://doi.org/10.1111/j.1751-908X.1995.tb00147.x

Wilkinson JFG (1977) Analcime phenocrysts in a vitrophyric analcimite-primary or secondary. Contrib Mineral Petrol 64:1–10

Wilson M (1989) Igneous petrogenesis: a global tectonic approach. Chapman & Hall, London, p 446

Wotzlaw JF, Husing SK, Hilgen FJ, Schaltegger U (2014) High-precision zircon U-Pb geochronology of astronomically dated volcanic ash beds from the Mediterranean Miocene. Earth Plane Sci Lett 407:19–34

Xiao L, Clemens JD (2007) Origin of potassic (C-type) adakite magmas: experimental and field constraints. Lithos 95:399–414

Xie Q, Zhang Z, Campos E, Cheng Z, Fei X, Liu B, Qiu Y, Santosh M, Ke S, Xu L (2018) Magnesium isotopic composition of continental arc andesites and the implications: a case study from the El Laco volcanic complex, Chile. Lithos 318–319:91–103

Xu JF, Shinjo R, Defant MJ, Wang Q, Rapp RP (2002) Origin of Mesozoic adakitic intrusive rocks in the Ningzhen area of east China: partial melting of delaminated lower continental crust? Geology 30:1111–1114

Yeganehfar H, Ghorbani MR, Shinjo R, Ghaderi M (2013) Magmatic and geodynamic evolution of Urumieh– Dokhtar basic volcanism, Central Iran: Major, trace element, isotopic, and geochronologic implications. Int Geol Rev 55(6):767–786

Yuan L, Zhang X, Xue F, Lu Y, Zong K (2016) Late Permian high-Mg andesite and basalt association from northern Liaoning, North China: insights into the final closure of the Paleo-Asian Ocean and the orogen–craton boundary. Lithos 258–259:58–76

Zhang Q, Wang Y, Qian Q, Yang JH, Wang YL, Zhao TP, Guo GJ (2001) The characteristics and tectonic–metallogenic significances of the adakites in Yanshan period from eastern China. Acta Petrol Sin 17:236–244

Zindler A, Hart SR (1986) Chemical geodynamics. Annu Rev Earth Planet Sci 14:493–571